Fakultät für Physik und Astronomie
Ruprecht-Karls-Universität Heidelberg

MASTERARBEIT

im Studiengang Physik

vorgelegt von

Tobias Schmitt

aus Weinheim

2019

Calorimetric Measurement of the ^{193}Pt Electron Capture Spectrum

Die Masterarbeit wurde von Tobias Schmitt
ausgeführt am
Kirchhoff-Institut für Physik
unter der Betreuung von
Frau jProf. Dr. L. Gastaldo

The determination of the absolute scale of neutrino masses is a major challenge in particle physics. One experimental route pursued to to solve this challenge is the analysis of the electron capture decay in ^{163}Ho, as for example done by the ECHo experiment. Those experiments rely on a precise theoretical description of the electron capture spectrum. To support the development of future theories, high resolution and high statistic measurements of different electron capture spectra are necessary. In this work the electron capture spectrum of ^{193}Pt was measured be enclosing ^{193}Pt in the absorbers of a detector array of metallic magnetic calorimeters. The detector chip was characterized and used to measure a first ^{193}Pt spectrum. An external 55 Fe x-ray source was used to calibrate the energy scale and extract the peak energies of the ^{193}Pt lines. The detector showed a moderate energy resolution of 21 eV (FWHM) due to a weak thermal contact leading to an effective operation temperature of 40 mK. A detailed activity analysis of the implanted pixel was performed and a lower than expected ^{193}Pt activity of up to 35 mBq found. The results obtained in this work demonstrate that the detectors enclosing ^{193}Pt are performing according to expectation. This suggests that improving the detector setup to reach a better cooling of the detectors will allow for performing a high energy resolution measurement of the ^{193}Pt EC spectrum.

Kalorimetrische Messung des Energiespektrums des Elektroneneinfangzerfalls von ^{193}Pt

Die Größenordnungsbestimmung der Neutrinomassen ist gegenwärtig eine zentrale Herausforderung der Teilchenphysik. Eine experimentelle Herangehensweise zur Lösung dieses Problems, ist die Analyse des Endpunkts des Zerfallsspektrums von ^{163}Ho, welches unter Elektroneneinfang zerfällt. Dieser Ansatz wird zum Beispiel vom ECHo Experiment verfolgt. Derartige Experimente sind auf eine akkurate theoretische Beschreibung des Energiespektrums angewiesen. Daher sind hochaufgelöste Messungen der Energiespektren weiter Elektroneneinfangszerfälle mit aussagekräftiger Statistik notwendig um die Entwicklung solcher Theorien zu unterstützen. In dieser Arbeit wurde das Energiespektrum des Elektroneneinfangzerfalls von ^{193}Pt gemessen. Dafür wurde das Zerfallsmaterial in den Absorbern eines Detektorarrays von Metallisch Magnetischen Kalorimetern eingeschlossen. Der Detektor wurde charakterisiert und anschließen ein ein erstes ^{193}Pt Elektroneneinfangspektrum gemessen. Hierbei wurde eine externe ^{55}Fe Röntgenquelle zwecks Energiekalibrierung verwendet um die Mittelpunktsenergien der ^{193}Pt Linien zu bestimmen. Der Detektor zeigte eine moderate Energieauflösung mit einer Halbwertsbreite von 21 eV. Dies lag an einer zu geringen thermischen Leitfähigkeit zwischen Detektor und Kryostaten, die eine Betriebstemperatur des Detektors von 40 mK zur Folge hatte. Weiterhin wurde die ^{193}Pt Aktivität in implantierten Pixel bestimmt, die mit einem Maximalwert von 35 mBq niedriger lag als erwartet. Die Ergebnisse dieser Arbeit bestätigen die Funktionsweise des ^{193}Pt implantierten Detektors. Weiterhin lässt sich schlussfolgern, dass eine Verbesserung der Kühlung des Detektors bereits ausreicht um ein hochaufgelöstes Energiespektrum des Elektroneneinfangzerfalls von ^{193}Pt zu messen.

Table of Contents

1 Introduction **1**

2 Electron Capture, Neutrino Mass and the ECHo Experiment **3**

2.1 Electron Capture and the Neutrino Mass 3

2.2 The ^{163}Ho EC Spectrum 6

2.3 Test theoretical models on low energy EC spectra 9

3 Metallic Magnetic Calorimeters **13**

3.1 Gradiometric Detector Design 14

3.2 SQUID readout 15

4 Experimental Setup **21**

4.1 The *maXs30* MMC array 21

4.2 Additional Absorber Layer 25

4.3 Implantation and Post Processing 26

4.4 Experiment Setup 30

4.5 ^{55}Fe calibration source 34

5 Experimental Results **35**

5.1 Chip Characterization and Noise Measurement 35

5.2 Pulse Shape Analysis 37

5.3 Measurement of the ^{193}Pt EC Spectrum 41

6 Summary and Outlook **51**

Literaturverzeichnis **55**

1. Introduction

Neutrinos are puzzling many physicists since decades and are presently considered one of the most important system to investigate physics beyond the standard model of particle physics. The discovery of neutrino oscillations demonstrated that neutrinos are massive particles nonetheless the mass mass scale of neutrinos is still unknown. Several observables can be studied to gain information on the mass of neutrinos. The analysis of low energy EC and β decay provides a model independent approach for the determination of the effective electron neutrino mass, since it relies only on energy and momentum conservation. The analysis of electron capture (EC) spectra was already proposed in the early 1980s, with ^{163}Ho being the best suited nuclide to carry out such an analysis. The ECHo experiment is one of those that aims to determine the neutrino mass by analysing the endpoint region of the ^{163}Ho EC spectrum.

To gain robust results from such an analysis, a good understanding of the spectral shape is essential. Precise measurements of the ^{163}Ho spectrum performed by the ECHo collaboration pointed out that there is no working theoretical description of the ^{163}Ho spectrum, let alone a general one for a multitude of EC unstable isotopes. Strong efforts are made to develop such a general description of EC spectra on just the basis of fundamental principles of nuclear and atomic physics. High resolution, high statistics measurements of different EC spectra are necessary to validate those theoretical approaches. A test of the theoretical approach used for the description of ^{163}Ho EC spectrum would be to apply the same method to describe other low energy EC spectra. One of the best candidates for such a measurement is the platinum isotope ^{193}Pt, which has an energy available for the decay of $Q_{\mathrm{EC}} = 56.6\,\mathrm{keV}$ allowing for capture from the L-shell.

The subject of this thesis is the realization of an experimental setup for the measurement of a ^{193}Pt EC spectrum. ^{193}Pt was enclosed in the absorbers of magnetic metallic calorimeters, the same approach used by ECHo for ^{163}Ho. After fabricated, the detector array was characterized and the activity of the enclosed source analyzed. A first measurement of a ^{193}Pt EC spectrum was performed with the final setup.

Chapter 2 gives an introduction to the EC process, as well as its connection to the neutrino mass. The basic principles of a simple description of the spectral shape are discussed and compared to experimental data. Further, the decision to measure the EC spectrum of ^{193}Pt is motivated in detail and discussed in the light of previous measurements.

Chapter 3 introduces the concept and working principle of metallic magnetic calorimeters, the low temperature detectors used in the framework of this thesis. It introduces some fundamental design principles and read out concepts.

Chapter 4 starts out with a description of the utilized detector array, the *maXs30*. Original state, as well as the modifications, in particular the challenges in the fabrication of the 4π absorbers are explained in detail. This includes the developed process of fully encapsulating the ion-implanted source in the detectors absorber. The experimental setup designed for measuring the chip with ^{193}Pt is presented. Additionally a brief overview on the ^{55}Fe calibration source is given.

Chapter 5 gives an overview of the functionality of the detector chip. A qualitative and quantitative analysis of signal shape is carried out and compared to the expected behaviour. From there, insights on the actual temperature on the chip during the experiment are gained and used to obtain an expected energy resolution of the detector. Subsequently, the methods of data analysis are discussed. Finally, the measured EC spectrum of ^{193}Pt is presented. This is concluded by a detailed analysis of the activity of implanted ^{193}Pt in the different detectors. Finally, expectations for a future experiment are finally discussed.

Chapter 6 gives a summary of this thesis.

2. Electron Capture, Neutrino Mass and the ECHo Experiment

Ever since the postulation by Wolfgang Pauli in 1930 [Pau77], neutrinos keep posing a challenge for experimentalists. Though the discovery of neutrino oscillations [Fuk98, Ahm02] provided a tool to measure the mass differences of the different neutrino mass eigenstates [Fog11], the absolute scale of neutrino masses remains unknown. One of the vastly different approaches to gain knowledge on neutrino masses is the analysis of kinematics of weak interaction processes, like β- or electron capture (EC) decay. In both processes an electron (anti)neutrino is emitted, which is typically not measured. Therefore the shape of the measured energy spectrum carries information on the emitted neutrinos, given a fixed energy for the decay Q. This analysis is based only on the energy and momentum conservation and therefore this approach is considered to be independent of theoretic models describing the physics of the neutrino. There are several experiments pursuing this route, that seek to measure the effective neutrino mass (from now on only referred to as neutrino mass) by analysing the kinematics of low energy EC and β processes. The ECHo experiment is one of those and performs a calorimetric measurement of the ^{163}Ho EC energy spectrum [Gas17].

2.1 Electron Capture and the Neutrino Mass

Electron capture is a radioactive decay, which was first observed by [Alv37]. It is a weak nuclear process occurring in atoms with an excess of protons, often together with β^+-decay (only if the total available energy allows β^+-decay). Hence it is often included as a type of beta decay. Figure 2.1 shows a sketch of this process: An electron is captured, typically from an inner shell, in the nucleus where a proton turns into a neutron. To conserve the lepton number, an electron neutrino is created:

$$\begin{aligned} {}^{\mathrm{A}}_{\mathrm{Z}}\mathrm{X} &\longrightarrow {}^{\mathrm{A}}_{\mathrm{Z-1}}\mathrm{Y}^* + \nu_{\mathrm{e}} \\ {}^{\mathrm{A}}_{\mathrm{Z-1}}\mathrm{Y}^* &\longrightarrow {}^{\mathrm{A}}_{\mathrm{Z-1}}\mathrm{Y} + E \end{aligned} \tag{2.1}$$

For decays to the nuclear ground state, the daughter nuclide is left in an atomic excited state Y^* and de-excites by emitting x-rays and/or Auger-electrons. For a capture to occur from a specific shell or electron state, there must be an overlap of the electronic wave function with the nucleus and the capture must be energetically possible. This means for example, that capture form bound states can only occur,

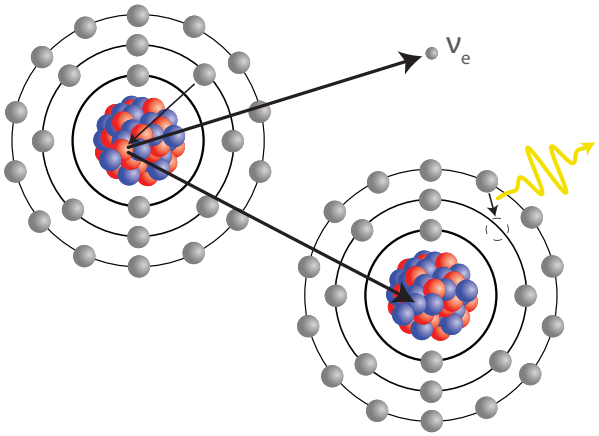

Fig. 2.1: Schematic of an electron capture process. An electron (grey), whose wave function has an overlap with the core, is captured there and together with a proton (red) forms a neutron (blue) and an electron neutrino (ν_e), as in Equation 2.1. While the neutrino escapes and caries away some of the energy, the daughter nuclide is left in an excited state. It de-excites via dipole radiation or the Auger-Meitner process.

when the binding energy of the electron is smaller than the total energy difference between mother and daughter nuclide, the so called Q-value Q_{EC}. The energy available for this decay is split between the created neutrino and the daughter nuclide, which is left with the Energy E in an excited state mainly due to the presence of the vacancy left by the captured electron.

This leads to the fact that both EC and beta spectra depend on the neutrino phase space term, which in turn contains the information on the effective mass.

Spectral Shape

The energy E that remains in the system and is not carried away by the neutrino is split in nuclear recoil and an excitation of the electronic system of the daughter atom. For high mass atomic system (which holds for all EC processes discussed in this thesis), the nuclear recoil is negligible and we may only consider the electronic excitation for now. In particular in case of low neutrino energy near the endpoint of the spectrum this approximation is valid.

We consider an experiment in which all the energy left in the daughter atom can be simultaneously measured if it is emitted via x-rays or electrons. Then the energy spectrum can be described by a sum of Breit-Wigner-resonances, one for each excited

state H in which the daughter atom can be left in, with corresponding energy E_H:

$$\frac{\mathrm{d}N}{\mathrm{d}E} \propto \sum_H n_H B_H \phi_H^2(R) \frac{\Gamma_H/2\pi}{\left(E - E_H\right)^2 + \Gamma_H^2/4} \tag{2.2}$$

Γ_H is the intrinsic linewidth of each resonance, while $\Phi_H(R)$ is the corresponding electronic wave function for the mother nuclide evaluated at the radius of the nucleus R. The occupancy is given by n_H, while B_H includes overlap between electron wave functions of mother and daughter atom and corrections due to exchange between their energy eigenstates.

Further, the sum of resonances has to be multiplied with the phase space factor of the emitted neutrino. This term depends on the effective electron neutrino mass $m(\nu_\mathrm{e})$ and total available energy Q_EC. While in theory the phase space depends on the masses of all three mass eigenstates of the neutrino, these deviations would be too small compared to any expected detector resolution. Hence, we can use a single effective neutrino mass $m(\nu_\mathrm{e})$ given via the PMNS-matrix elements $|u_{\mathrm{e}i}|^2$ and the following equation:

$$m(\nu_\mathrm{e}) = \sqrt{\sum_{i=1}^{3} |u_{\mathrm{e}i}|^2 m_i^2} \tag{2.3}$$

Using this, we can add the phase space prefactor to Equation 2.2 and therefore the function describing the spectral shape of EC decay is

$$\frac{\mathrm{d}N}{\mathrm{d}E} \propto \left(Q_\mathrm{EC} - E\right)^2 \sqrt{1 - \left(\frac{m(\nu_\mathrm{e})}{Q_\mathrm{EC} - E}\right)^2} \sum_H n_H B_H \phi_H^2(R) \frac{\Gamma_H/2\pi}{\left(E - E_H\right)^2 + \Gamma_H^2/4}. \tag{2.4}$$

The greatest effect of a finite neutrino mass is just below the endpoint of the spectrum, as is clear from the phase space factor. A suitable decay to study this effect should hence show a high spectral weight within the last few eV below the endpoint. This is maximized for two important decay characteristics: First, a low Q-value increases the fraction of events in a region of interest just below Q_EC. Mathematically this results from the first term of the phase space factor $\left(Q_\mathrm{EC} - E\right)^2$ in Equation 2.4 and normalization. Second, a major atomic resonance just at or below the Q-value increases the capture probability there, as shown in Equation 2.2, but no nuclide with $E_H \approx Q_\mathrm{EC}$ has been found yet. From the known nuclides that undergo EC, ^{163}Ho fulfills these requirements best.

2.2 The ^{163}Ho EC Spectrum

The holmium isotope ^{163}Ho decays via EC to the dysprosium isotope ^{163}Dy:

$$\begin{aligned} {}^{163}_{67}\mathrm{Ho} &\longrightarrow {}^{163}_{66}\mathrm{Dy}^{*} + \nu_{\mathrm{e}} \\ {}^{163}_{66}\mathrm{Dy}^{*} &\longrightarrow {}^{163}_{66}\mathrm{Dy} + E \end{aligned} \tag{2.5}$$

This process has a rather low Q-value of $Q_{\mathrm{EC}} = 2833\,(30_{\mathrm{stat}})\,(15_{\mathrm{sys}})\,\mathrm{eV}$ [Eli15], which is the smallest among all known EC unstable nuclides and a large half-life of $T_{1/2} = 4570(15)\,\mathrm{yr}$ [Bai83]. As a result, a number of about 2×10^{11} atoms is necessary to achieve an activity of 1 Bq.

Due to the low Q-value the ^{163}Ho spectrum consists of only seven first order transitions. These lines are: MI (capture from $3s$), MII ($3p_{1/2}$), NI ($4s$), NII ($4p_{1/2}$), OI ($5s$), OII ($5p_{1/2}$), PI ($6s$) for ^{163}Ho in pure form. Incorporated in a host metal, the $6s$ electron are in a valence band and therefor their capture might be suppressed. Energies and natural linewidths for the 5 higher energetic lines are given in Table 2.1 together with source references. Figure 2.2 left shows the spectral shape obtained by plugging the peak energies and corresponding intrinsic widths, as well as the Q-value in Equation 2.4 for different neutrino masses. The spectral shape over the full energy range does not show a great sensitivity on the neutrino mass on first glance. In the endpoint region of the spectrum, which Figure 2.2 right shows a zoom in on, the spectrum varies significantly with different values for the neutrino mass, as was expected from the shape of the phase space factor in Equation 2.4.

The ECHo Experiment

The ECHo Experiment [Gas17] is designed to measure the electron neutrino mass by analyzing the calorimetically measured spectrum of the ^{163}Ho EC decay. To achieve this, ^{163}Ho is enclosed in metallic magnetic calorimeters via ion implantation (see also chapter 3). Currently, the experiments is running the first science phase, called ECHo-1k. Here, the goal to measure an activity of 1 kBq of ^{163}Ho with a MMC array of about 100 pixels. With such an experiment, a sensitivity on the neutrino mass below 10 eV can be reached. The following phase, for which research and development is already going on, will measure large arrays for a total of about 12000 pixels, each with 10 Bq of ^{163}Ho enclosed in the MMC absorber. With such an experiment, a sensitivity of about 1 eV or even below will be reached.

Experimental Observations

Figure 2.3 shows an energy spectrum which was calorimetically measured with the ECHo experiment, with an simple theory approach overlayed. The shape of the ^{163}Ho

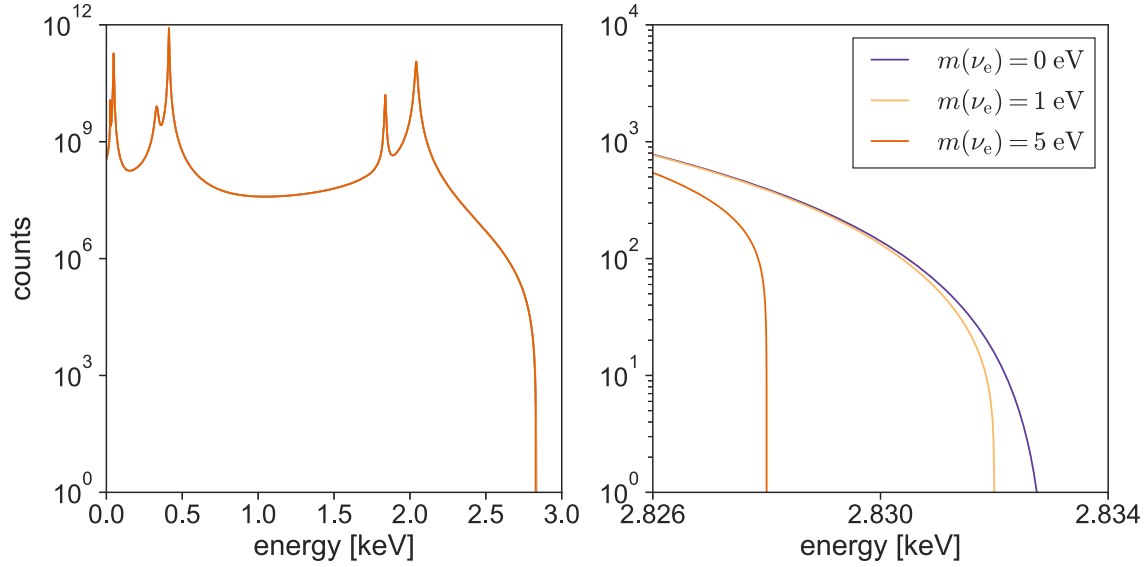

Fig. 2.2: Left: A first order calculation of the ^{163}Ho spectrum according to Equation 2.4 for different neutrino masses. On the full energy scale, no deviation for different neutrino masses can be appreciated. Right: Zoom in on the endpoint region of the spectrum. Differences in the spectral shape for different neutrino masses are clearly visible there.

spectrum is obtained by considering only first order excitations using Equation 2.4 with the input of the main resonance lines given in Table 2.1. While the rough spectral shape at the level of the main peaks does fit the experimental observations, especially in the region between 0.5 keV and 1.5 keV does deviate significantly. In particular substructures are observed at 0.5 keV, as well as continuous tails extending on the high energy sides of the two main resonance clusters. These structures can not be interpreted as external background, but point to the need of a more detailed description of the electron capture process.

When aiming to draw precise conclusions from small scale deviations of the spectrum, as expected for a specific neutrino mass (as can be seen in Figure 2.2), a good understanding of the spectral shape is necessary.In particular defines the phase space factor of the energy spectrum the region of interest for the determination of the neutrino mass close to the endpoint (about 100 eV below the Q-value) The observation of small discrepencies between existing theoretical models and experimental data has motivated theorists to predict the shape of the ^{163}Ho spectrum [Rob15, Rob15, DR16] with more eloberated models. In General improving on this descriptions on a phenomenological way and tailoring any description specifically to just the ^{163}Ho would undermine the credibility of any result later retrieved based on this description. Hencenew *ab-initio* approaches, that aim to calculate the complete atomic spectral shape including all relevant processes from first principles, are a promising solution to this problem. In the following the *ab-initio* approach used in

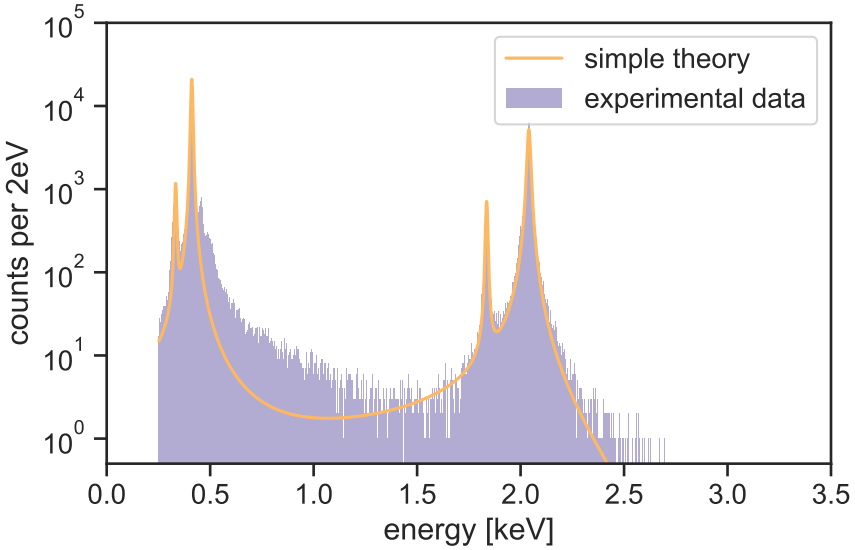

Fig. 2.3: Comparison of a calorimetric measurement of the ^{163}Ho EC spectrum and a simple theory as given by Equation 2.4 and the values in Table 2.1. The most obvious difference is the structure above the NI line at about 0.5 keV, that is missing in the theoretical description.

[Bra18] will be introduced and the achieved agreement with the measured spectra will be discussed.

New theoretical Approaches

Figure 2.4 shows this theoretical description next to a simple approach as given by Equation 2.4 and experimental data. An overview over the full energy range is given on the left, while on the right a zoom in on the N-line is presented. While the new approach still has problems to reproduce the exact line positions, it hints on possible reasons for some of the unexplained substructure. Such reasons include effects like the transfer of core hole excitations via coulomb repulsion with the valence shell to levels where the capture process itself is not possible or shake-up processes, where a core electron is transferred into the valence shell and the atom is left with two core holes. The size of the NII resonance line which could not be described considering only a single Lorentzian centerd at 0.33 keV with a width of 5.3 eV is well motivated within the ab initio theory because of the presence of a large multiplet. Nevretheless the continuum tales between 0.6 keV and 1 keV are still not described. To achieve a better agreement transitions to the continuum need to be included in the model.

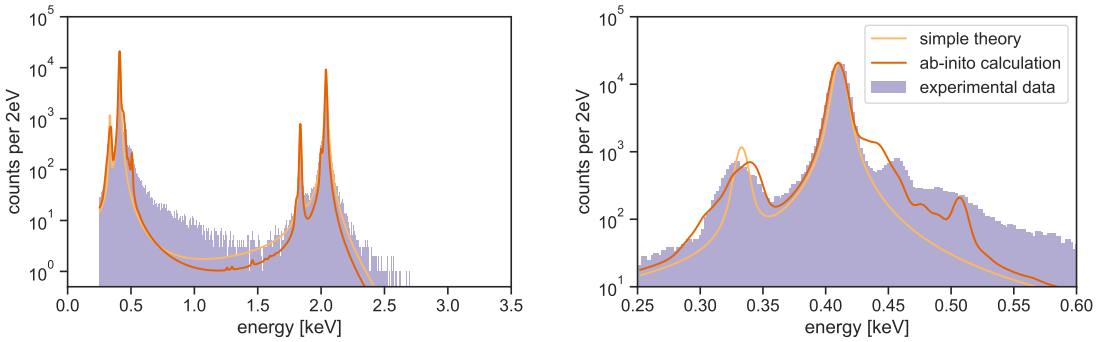

Fig. 2.4: Left: A new *ab-initio* approach to calculate the ^{163}Ho EC spectrum [Bra18], compared with a calorimentric measured spectrum and a simple theory approach as given by Equation 2.4 and the values in Table 2.1. Right: Zoom in on the N line. While the *ab-initio*, which uses no experimental input, does not reproduce the peak energies as precise, it hints on an existing structure above the NI line, which the simple theory approach can not describe.

2.3 Test theoretical models on low energy EC spectra

Recent theoretical models have already improved the description of the ^{163}Ho EC spectrum, as mentioned above. Already made, or currently worked on, extensions to those models, including decay to the continuum (x-ray and shake-off processes) and describing the effect of having ^{163}Ho in a solid structure, promise to reach a very good theoretical understanding of the experimental observations.

In order to prove the generality of these theoretical models and calculations, the possibility to test them for the description of EC spectra of different isotopes than ^{163}Ho would be of great importance. A well working *ab-initio* approach should be able to reproduce also other EC spectra. Such a comparison would proof that the EC process can be precisely modelled. This would ensure the reliability of the prediction of the spectral shape of ^{163}Ho at the end-point region and therefore strengthen any conclusion drawn from spectral analysis in this energy rang.

Using the criterion, that the nuclides for this test should be of comparable mass as ^{163}Ho and have a low Q-value, there are two major candidates for testing a theoretical description on low energy EC spectra: The platinum isotope ^{193}Pt and the terbium isotope ^{157}Tb. While the low Q-value of ^{163}Ho does not allow for capture from the first (K-line) or second (L-line) shell, ^{163}Pt due to its Q-value of $Q_{\mathrm{EC}} = 56.6\,\mathrm{keV}$ [SB17] allows for second shell capture. ^{157}Tb has a Q-value of $Q_{\mathrm{EC}} = 62.8\,\mathrm{keV}$ [Wap85] and therefore capture from the first shell occurs. The half-life times for the electron capture in ^{193}Pt and ^{157}Tb are with $T_{1/2} = 50\,\mathrm{yr}$ for ^{193}Pt and with $T_{1/2} = 150\,\mathrm{yr}$ for ^{157}Tb (both taken from [Kel83]) rather low compared to the half-life of the ^{163}Ho

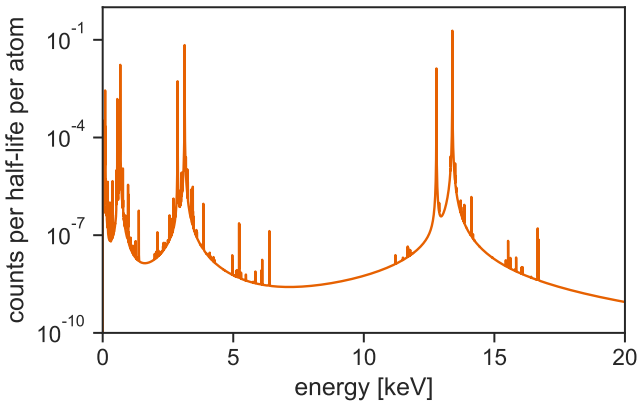

Fig. 2.5: Preliminary calculation of the ^{193}Pt EC spectrum (from Martin Brass, private communication). Everything above 20 keV up to the endpoint was omitted, since there are no further spectral features.

EC decay. This has as experimental consequence a great reduction of the amount of implanted atoms needed to reach the same activity.

In the framework of this thesis, the EC spectrum ^{193}Pt was investigated. ^{193}Pt decays into the iridium isotope ^{193}Ir through the following scheme:

$$\begin{aligned} {}^{193}_{78}\mathrm{Pt} &\longrightarrow {}^{193}_{77}\mathrm{Ir}^{*} + \nu_{\mathrm{e}} \\ {}^{193}_{77}\mathrm{Ir}^{*} &\longrightarrow {}^{193}_{77}\mathrm{Ir} + E \end{aligned} \tag{2.6}$$

Figure 2.5 shows a preliminary calculation of the ^{193}Pt EC spectrum. Apart from the main lines several smaller spectral features are predicted in the energy range below 20 keV. Above that, there are no major resonances or spectral features. The K-line would be situated at around 62.7 keV, which is above the Q_{EC}-value of 56.6 keV. Further, in Table 2.2 literature values for some major resonance lines of ^{193}Pt are given.

Previous Measurements of ^{193}Pt EC spectra and motivation for this work

Recently a group at LANL performed a calorimetric measurement of the ^{193}Pt EC spectrum utilizing a transition edge sensor to measure the temperature change of an absorber containing ^{193}Pt [Koe18]. The achieved energy resolution was 52 eV(FWHM). Figure 2.6 shows the result of this measurement. Several lines of contaminants are visible, especially from ^{192}Ir.

The energy calibration was a single point calibration at the L1-line of ^{193}Pt itself. The absorber was produced by irradiating a ^{192}Pt enriched platinum foil with ther-

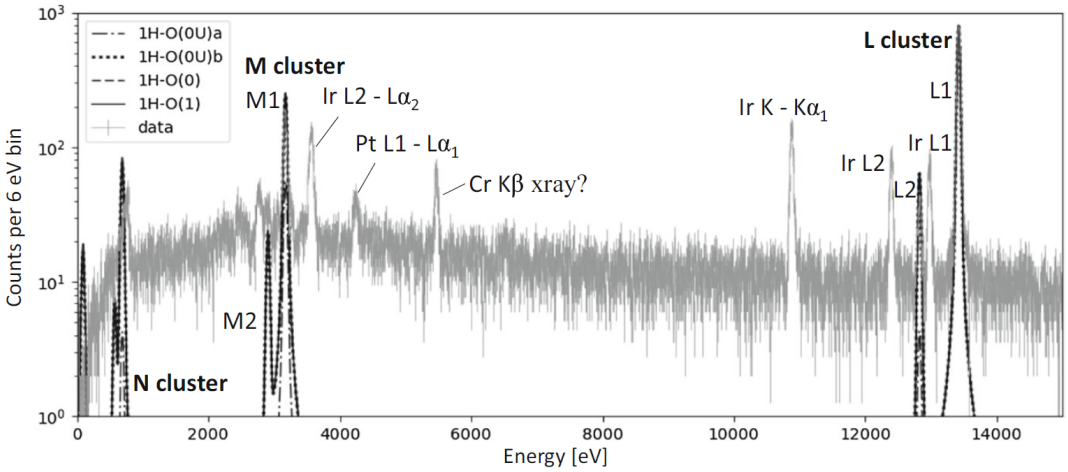

Fig. 2.6: First calorimetric measurement of the ^{193}Pt EC spectrum as reported by [Koe18]. Several lines caused by contamination are visible, especially also around the L line of ^{193}Pt. Two resonances of ^{192}Ir are present in the same energy region.

mal neutrons. While this ensures a simple absorber/source matrix structure and a homogeneous distribution of ^{193}Pt, it also results in a less than ideal enclosure of the source: Since ^{193}Pt is also created near the surface, parts of the released energy E may escape especially for released x-ray radiation. This would then result in wrong intensity ratios for different lines of the spectrum. Further, this method of source preparation also created the contaminants like ^{192}Ir.

The aim of this thesis is to measure the ^{193}Pt EC spectrum with high energy resolution using a detector in which ^{193}Pt is localized in the center of a 4π geometry. In addition an external calibration source will be used to enable absolute and not only relative measurements of the peak energies. The exact positions of the lines are of key importance for testing the quality of *ab initio* calculations. Finally this thesis aims to proof that metallic magnetic calorimeters with ^{193}Pt implanted in the energy absorber can fulfill the requirements for a precise measurement of the ^{193}Pt spectrum.

Tab. 2.1: Binding energies E^{lit} of electrons in ^{163}Dy and corresponding natural linewidths Γ^{lit}. The experimental values E^{exp} and Γ^{exp} for a calorimetric measurement of ^{163}Ho enclosed in gold are given in comparison. Binding energies are taken from [Des03] and linewidths from [Cam01], except for the O1-line where the energy is taken from [Tho09] and the linewidth from [Coh72]. The experimental values were obtained by [Ran14].

Level	E^{lit} [eV]	Γ^{lit}[eV]	E^{exp} [eV]	Γ^{exp} [eV]
MI	2046.9	13.2	2040	13.4
MII	1844.6	6.0	1836	4.8
NI	420.3	5.4	411	4.7
NII	340.6	5.3	333	13.0
OI	49.9	3.7	48	5.6

Tab. 2.2: Binding energies E^{lit} of electrons in ^{193}Ir and corresponding natural linewidths Γ^{lit}. Binding energies are taken from [Des03] and linewidths from [Cam01].

Level	E^{lit} [eV]	Γ^{lit}[eV]
LI	13423.3	7.9
LII	12829.4	5.2
MI	3176.4	14.8
MII	2912.9	9.4
NI	699.1	8.0
NII	586.7	6.1

3. Metallic Magnetic Calorimeters

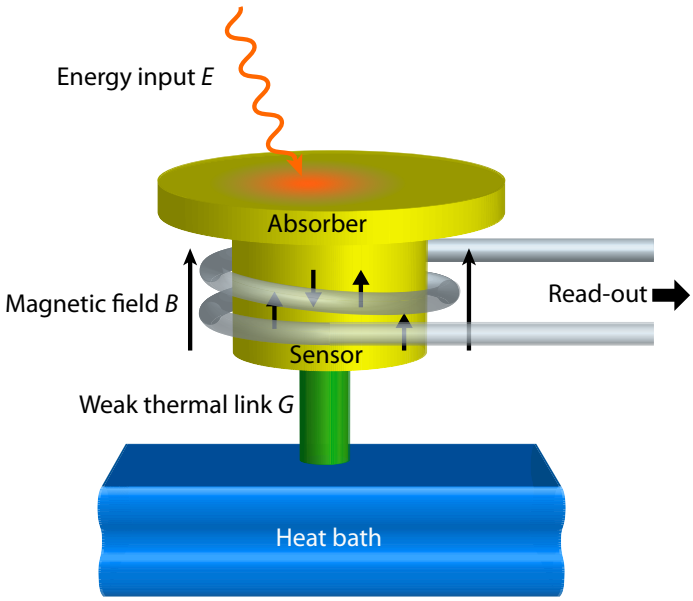

Fig. 3.1: Schematic drawing of a metallic magnetic calorimeter.

The detectors utilized in this thesis are based on the concept of metallic magnetic calorimeters (MMCs). The typical operating temperature of these detectors is in the range of 20 mK. Figure 3.1 shows a schematic of such a detector. It consist of an absorber and a paramagnetic sensor, which are in a strong thermal contact to each other. The sensor sits in an external magnetic field B and is coupled to an heat bath via a weak thermal link with thermal conductivity G. If now an energy input of magnitude E occurs in the absorber, the temperature of absorber and sensor increases according to:

$$\Delta T \approx \frac{E}{C_{\mathrm{tot}}} \tag{3.1}$$

Here ΔT denotes the change in temperature and C_{tot} denotes the total heat capacity of absorber and sensor together. The temperature of the detector then returns to its initial value following an exponential decay with a time constant τ of:

$$\tau = \frac{C_{\mathrm{tot}}}{G} \tag{3.2}$$

For small magnetic fields B, the paramagnetic sensor changes its magnetization M following a temperature change, according to the Curie law:

$$M \propto \frac{1}{T} \tag{3.3}$$

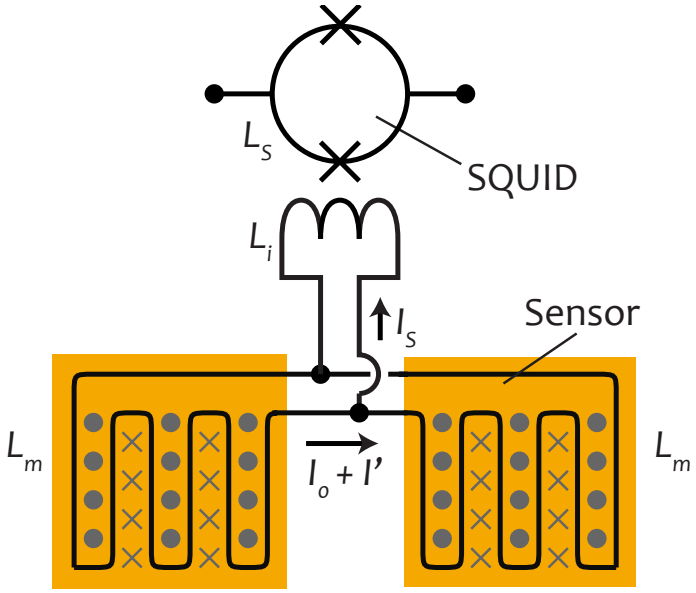

Fig. 3.2: Schematic view of the read-out geometry of the detector after [Fle05]. Two sensors on top of meander-shaped pick-up coils are arranged in a gradiometric configuration. The detector is coupled to the input coil of a SQUID current sensor. The magnetic field to polarize the paramagnetic sensors is generated by a persistent current I_0 flowing through the superconducting loop formed by the two meanders.

This change in magnetization is then related via the increase in temperature ΔT to the original energy input E:

$$\Delta M \propto \frac{\partial M}{\partial T}\Delta T \approx \frac{\partial M}{\partial T}\frac{E}{C_{\mathrm{tot}}} \tag{3.4}$$

The change in magnetization can be measured as a change in magnetic flux in a suitable designed superconducting pick-up coil and then converted into a Voltage with the use of superconducting quantum interference devices (SQUIDs). This will be described in section 3.2.

3.1 Gradiometric Detector Design

A typical way of implementing the detection principle of MMCs is a planar double meander geometry as depicted in Figure 3.2. The meanders are superconducting coils with an inductance L_{m}. They are both connected in parallel to the input coil L_{i} of a dc-SQUID. Directly on top of each meander is a paramagnetic sensor. This planar design allows for precise fabrication with standard lithography methods on a silicon wafer. By inserting a persistent current I_0 into the loop formed by the meanders, they also serve as the means to generate the external magnetic field, which is required to

polarize the sensor.

A change in magnetization in one of the sensor would now give rise to change in magnetic flux in the corresponding pick-up coil. But since the magnetic flux in a superconducting coil is conserved, it instead gives rise to a screening current that compensates this initial flux change. Using Kirchhoff's law and the conservation of flux in the individual coils as a additional condition, it is possible to calculate the corresponding current signal in the SQUID input coil:

$$\frac{\delta I_\mathrm{i}}{\delta \Phi} = \frac{1}{L_\mathrm{m} + 2\left(L_\mathrm{i} + L_\mathrm{p}\right)} \tag{3.5}$$

Here L_p denotes an additional parasitic inductance in series with the input coil due to the aluminium bonding wires between detector chip and SQUID chip.

There are two advantages of this gradiometric geometry: First, it allows to distinguish between signal occurring in the two sensors by the polarity of the pulse. In fact, the current signal I_s in the SQUID input coil changes direction for a signal in the two sensors respectively. Second, and as a direct result from the first one, the same temperature change in both sensors at the same time gives rise to two opposite signals, which cancel each other out. This makes the detector rather insensitive to fluctuations in the substrate temperature.

3.2 SQUID readout

DC-SQUID[1] current sensors can provide the necessary accuracy to read out the small changes in magnetic flux due to the tiny screening currents which are flowing through the input coil after an energy release in the detector as described above. They are explained in detail in [Cla04]. Here, the basic principles of a two-stage dc-SQUID current sensor setup, as used for the readout of MMCs are summarized.

Figure 3.3a shows a schematic of a dc-SQUID. It consists of a superconducting loop which is interrupted at two points by Josephson junctions. A Josephson junction is typically implemented in the form of a thin (in the order of a few nm) tunneling barrier made of a dielectric material. Its transport properties are governed the Josephson equations [Jos62]. The junctions allow flux to enter or leave the superconducting loop. The junctions are shunted to avoid hysteric effects.

If a dc-SQUID is operated in a setup as shown in Figure 3.3a, no voltage drop is observed for a bias current I_B below a critical current I_c defined by the junction geometry, since the Cooper pairs can still tunnel through the junction. Once the bias current exceeds this certain critical current I_c, then the current can no longer

[1] Superconducting Quantum Interference Device

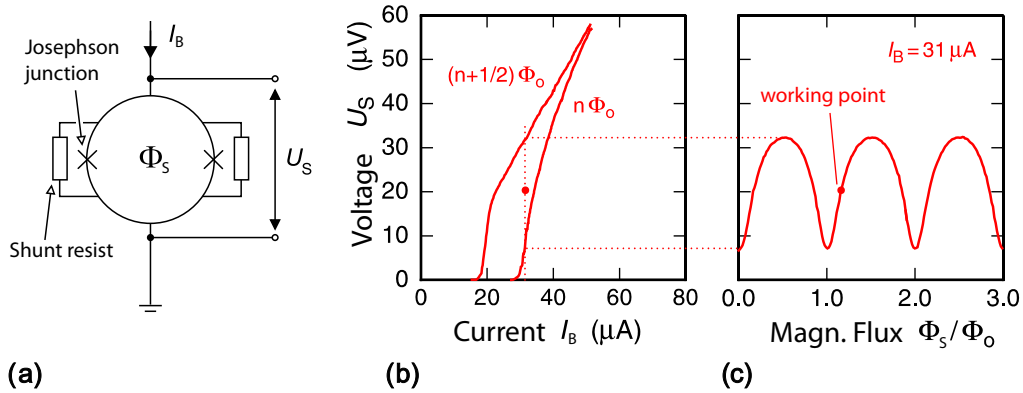

Fig. 3.3: (a) Schematic of a dc-SQUID. (b) Corresponding current-voltage characteristic for fluxes $\Phi_S = n\Phi_0$ and $\Phi_S = \left(n + \frac{1}{2}\right)\Phi_0$. (c) Voltage drop across the SQUID at a constant bias current I_B as a function of magnetic flux Φ_S. The matching bias current is also indicated in (b). From [Wei96]

.

be carried by Cooper pairs only, but also by quasi-particles that tunnel through the barrier. The voltage drop U_S becomes a function of the magnetic flux inside the superconducting loop for a given bias current. For a fixed bias current, this voltage drop is minimal for an integer multiple of the magnetic flux quantum $\Phi_0 \approx 2 \times 10^{-15}\,\mathrm{V\,s}$, meaning $\Phi_S = n\Phi_0$, with n being an integer. The voltage drop is maximal for half integer multiples: $\Phi_S = (n + 1/2)\Phi_0$. These two extremal curves are exemplary depicted in Figure 3.3b. If now the bias current I_B is fixed to a suitable value, we obtain a periodic flux dependent voltage drop U_S as can be seen in Figure 3.3c.

Since this flux-voltage characteristic of a dc-SQUID is highly nonlinear, the linear working range is reduced to about $\Phi_0/4$ and would be insufficient for most applications. In order to overcome this limitation, the SQUID is instead operated at a fixed working point, by inserting the output voltage in a closed feedback loop, in a scheme called flux-locked loop.

Flux-Locked Loop

Figure 3.4 shows the flux-locked loop (FLL) configuration. The general idea is to stabilize the SQUID in a suitable working point by compensating the flux changes in the SQUID via a feedback coil in a closed loop. This working point is chosen so that it provides a high sensitivity of the output voltage towards changes in magnetic flux, meaning a high value for $\partial U_S/\partial \Phi_S$.

The working point is defined by the bias current I_B and a reference voltage U_B. A change in magnetic flux $\delta\Phi_S$ in the SQUID leads to a change in Voltage δU_S. This

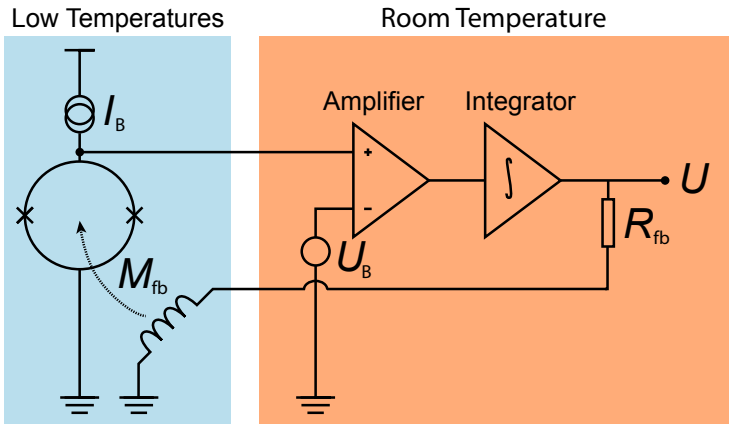

Fig. 3.4: Schematic of a FLL-circuit.

change is then amplified and integrated to an output voltage U, that also generates a feedback current I_{fb} via a feedback resistance R_{fb}. This feedback current flows through the feedback coil of the SQUID, which has a a mutual inductance M_{fb} with the SQUID-loop. This generates a magnetic flux Φ_{fb} within the SQUID that compensates the initial flux change $\delta\Phi_{\mathrm{S}}$:

$$\delta\Phi_{\mathrm{S}} = -\Phi_{\mathrm{fb}} = M_{\mathrm{fb}} I_{\mathrm{fb}} \tag{3.6}$$

The feedback current is directly related to the voltage drop U across the feedback resistance. This voltage provides an easy to measure signal proportional to the change in magnetic flux in the SQUID $\delta\Phi_{\mathrm{S}}$:

$$U = -\frac{R_{\mathrm{fb}}}{M_{\mathrm{fb}}} \delta\Phi_{\mathrm{S}} \tag{3.7}$$

Two-Stage Setup

While the above one-stage FLL setup achieves the goal of linearizing the SQUID output, it still suffers from a not negligible flux noise due to the presence of the room temperature electronics [2] that provide amplification and the bias current. The introduced noise of the electronics in the read-out chain is about $0.35\,\mathrm{nV}/\sqrt{\mathrm{Hz}}$. This effect can be reduced by the introduction of an additional amplifier stage at low temperatures.

Figure 3.5 depicts such a two-stage setup with an amplifier stage consisting of an array of dc-SQUIDs. This array is a series of N identical SQUIDs, which are set

[2] XXF-1 from Magnicon GmbH, Barkhausenweg 11, 22339 Hamburg, Germany

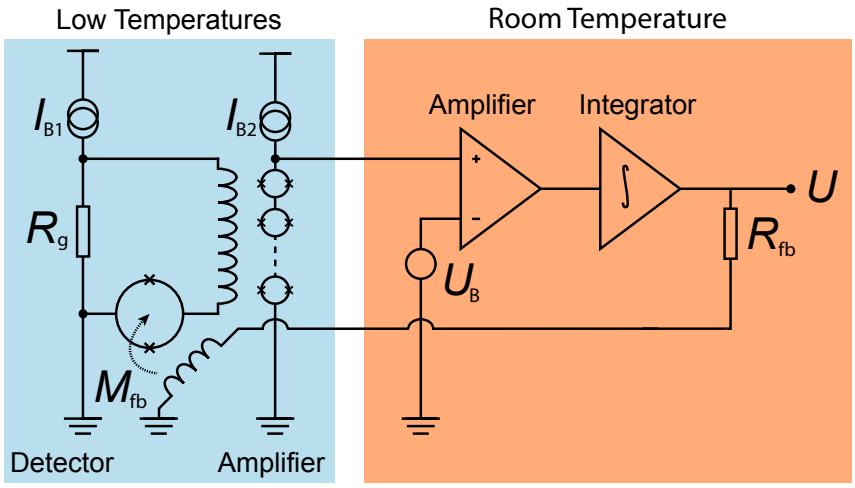

Fig. 3.5: Schematic drawing of the two-stage FLL circuit, which introduces a SQUID array as amplifier.

up so that their flux-voltage characteristic adds up coherently. If the same magnetic flux is coupled to all of them, they behave just like a single SQUID with an N-times larger output voltage U_S.

Further, the first-stage SQUID (or front-end SQUID) is operated in voltage bias mode. This is achieved by introducing a gain resistance R_g in parallel to the SQUID. For low values of R_g compared to the dynamic resistance of the SQUID, most of the bias current I_{B1} passes through the gain resistances and creates a voltage bias for the in parallel connected SQUID. Biased with this voltage, the current flow through the SQUID I_S now depends on the flux Φ_S. This current signal is used as an input for the amplifier SQUID array, which is operated in the standard current-biased mode discussed earlier in this section. It generates an output voltage, which is amplified and integrated to then establish a FLL, compensate the initial flux change in the front-end SQUID and generate the measured output voltage U.

Intrinsic SQUID Noise

The two-stage SQUID readout adds several contributions to the overall noise of the setup. This SQUID noise can be split into a white noise and frequency dependent $1/f$-component. In general the white noise introduced by the SQUID outweighs the frequency independent thermal noise contributed by the gain resistance R_g and the room temperature electronics.

Thermal noise of the shunt resistances (as depicted in Figure 3.3a) contributes the frequency independent part. The spectral power density $S^{SQ}_{\Phi,w}$ for a given resistance

R and temperature T, together with the Boltzmann constant k_B, is given by:

$$S_{\Phi,w}^{\mathrm{SQ}} = \frac{18 k_\mathrm{B} T L_\mathrm{S}^2}{R} \tag{3.8}$$

This holds for a SQUID with ideal geometry and inductance L_S [Tes77, Bru82].

At low frequencies the noise is dominated by frequency dependent component $S_{\Phi,1/f}^{\mathrm{SQ}}$ which behaves according to

$$S_{\Phi,1/f}^{\mathrm{SQ}} \propto \frac{1}{f^\xi} \tag{3.9}$$

with $\chi = 0.6 \ldots 1.2$ [Kem16]. While the exact origin of this noise contribution remains still unknown, one possible explanation are flipping magnetic moments on the surface of the SQUID loop, which might originate from adsorbates [Koc07].

4. Experimental Setup

4.1 The *maXs30* MMC array

The calorimetric measurements of the ^{193}Pt EC spectrum carried out in this work utilized a *maXs30* detector array. The *maXs30* is a 2D array of in total 32 double meander detectors with therefore 64 absorbers (also called pixels), which are placed in an 8x8 grid. The *maXs30* was developed for X-ray spectroscopy in the energy range up to 30 keV [Hen17].

Design

Figure 4.1 shows a technical drawing of the *maXs30* chip. On the left is a full overview of the complete chip with its edge length of 8 mm. The right-hand side shows a zoom on one of the four rotationally symmetric quadrants. The 64 gold absorbers (1) are located in the center of the chip. With an edge length of 500 µm per absorber square and a spacing of 20 µm in between two absorbers, the whole 8 by 8 grid covers a total area of about 17.15 mm^2 with 16 mm^2 being detection area. The detector is designed to support absorber thicknesses of 20-30 µm depending on the intended use. Below the absorbers are the para-magnetic sensors (2) made from Ag:Er with an edge length of 298 µm and a designed thickness of 3.5 µm. Absorber and sensor are connected via a set of three gold stems, that allow for a well defined thermal contact between them. The sensor is put on top the meander shaped pick-up coil that also provides the magnetic field via a persistent field current. They are galvanically separated by a SiO_2 insulation layer. The four large golden squares (3) with an edge length of 1 mm located close to the corners of the chip simply provide a visual aid when handling the chip and a resilient area to put pressure on the chip while, for example, gluing the chip on a holder. A pair of read-out lines (4) made of niobium goes to each detector, which consists of two pixels in a gradiometric setup as described in chapter 3. Field and heater current are each provided by a pair of niobium lines per quadrant (5). This means they connect eight detectors in series. All lines can be accessed at the rim of the chip via bond pads (6) for bonding wires (Aluminum with a diameter of 25 µm). The pads for field and heater lines are located in the corners, while the readout lines are along the edges of the chip, so that they line up nicely with the bonding pads of SQUID chips for first stage SQUIDs which will be placed alongside the detector chip.

Figure 4.2 shows a zoom on a single detector with its pixel pair in a gradiometric

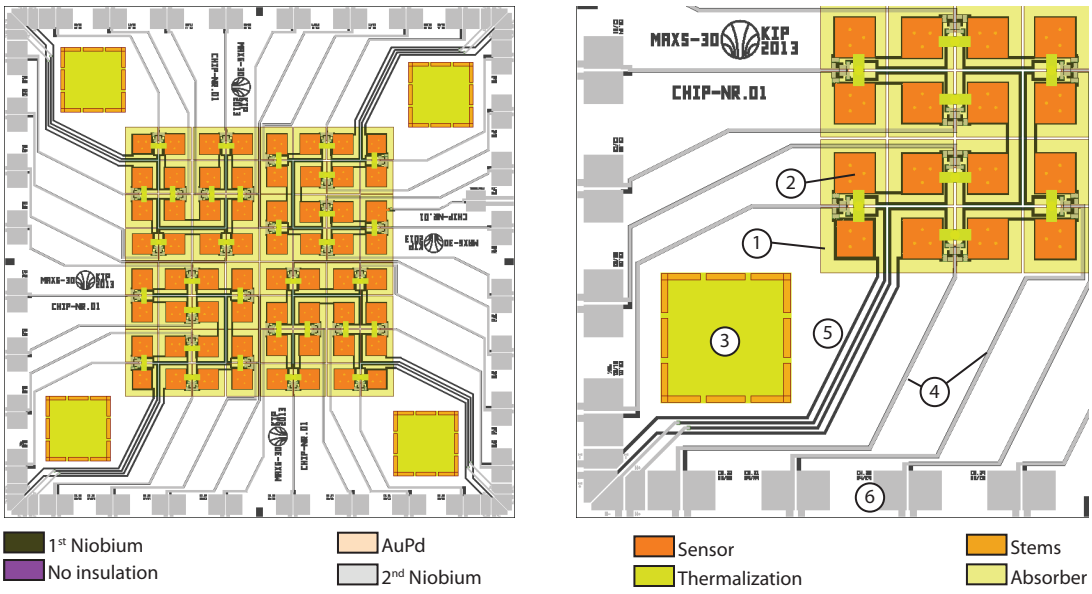

Fig. 4.1: Technical drawing of the *maXs30* chip. Material information is colour coded. The left-hand side is a full overview of the chip with its size of 8 mm by 8 mm, while the right-hand side provides as zoom in on one quadrant. (1) Absorber made from gold. The drawing is transparent so that wiring and sensor below are visible. (2) Thermal sensor made from Ag:Er. (3) Visual aids for handling of the chip. (4) Readout lines for one sensor pair each. (5) Lines for the persistent field current and heater current for the whole quadrant. (6) Bond pads to connect to the different lines via bonding wires.

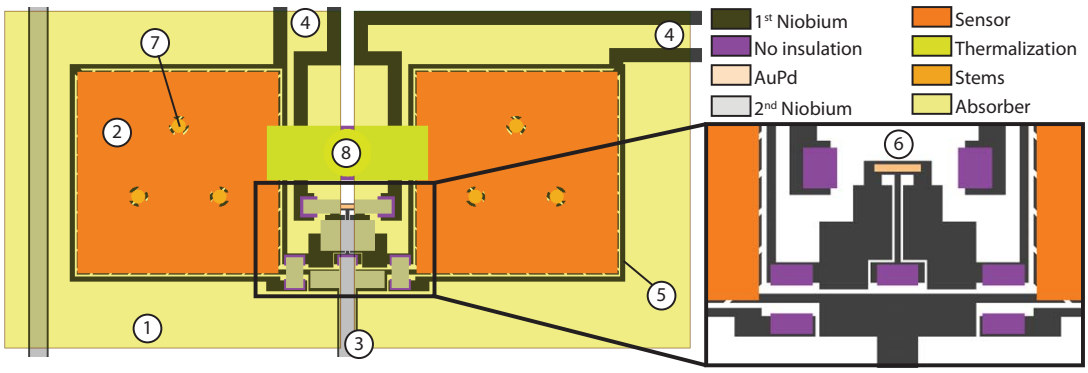

Fig. 4.2: Left: A single detector consisting of two pixels in a gradiometric setup. Right: Zoom in between the sensors. The second niobium layer is omitted here, to give a direct view on the underlying structure. (1) Absorber, drawn in transparent colour. (2) Paramagnetic sensor. (3) Read-out lines. (4) Lines for preparing the persistent current. (5) Meander and superconducting loop around it. (6) Heater to prepare the persistent current. (7) Stems on which the absorber sits. They fulfill a dual purpose in being also a thermal bottleneck between sensor and absorber. (8) Thermalization structure made from gold connecting both sensors.

setup. Apart from the absorbers (1) and sensors (2), the structure between the two pixels is also visible. This includes the connecting lines to the meander-shaped pick-up coil (3), the lines for field- and heater-current (4) to prepare the persistent field in the meander coils (5) using the gold-paladium heater (6), as well as the stems that separate absorber and sensor (7) and the mutual thermalization structure between the two sensors (8).

The utilized *maXs30* chip

The production and characterization of the first *maXs30* MMC-arrays is well documented in [Hen17]. A wafer of multiple detectors was fabricated up to the absorber layer, then diced and the individual detector chips stored away. The chip used to carry out this work is chip no. 16 of this batch and was partially tested before implantation. Figure 4.3 shows the state of the chip before implantation schematically. The lines for carrying the field current are broken in the first of the four quadrants, which renders all detectors there inoperable. Further two detectors (number 19 and 22) showed potentially broken read-out lines in a visual inspection with a microscope and might be defect.

Another important information from the characterization carried out in [Hen17] is the thickness of the absorbers. While the aimed for design value was 20-30 µm, the absorber thickness turned out thinner. The real absorber thickness was estimated to be 7(1) µm by the combination of three different measurements: optical analysis

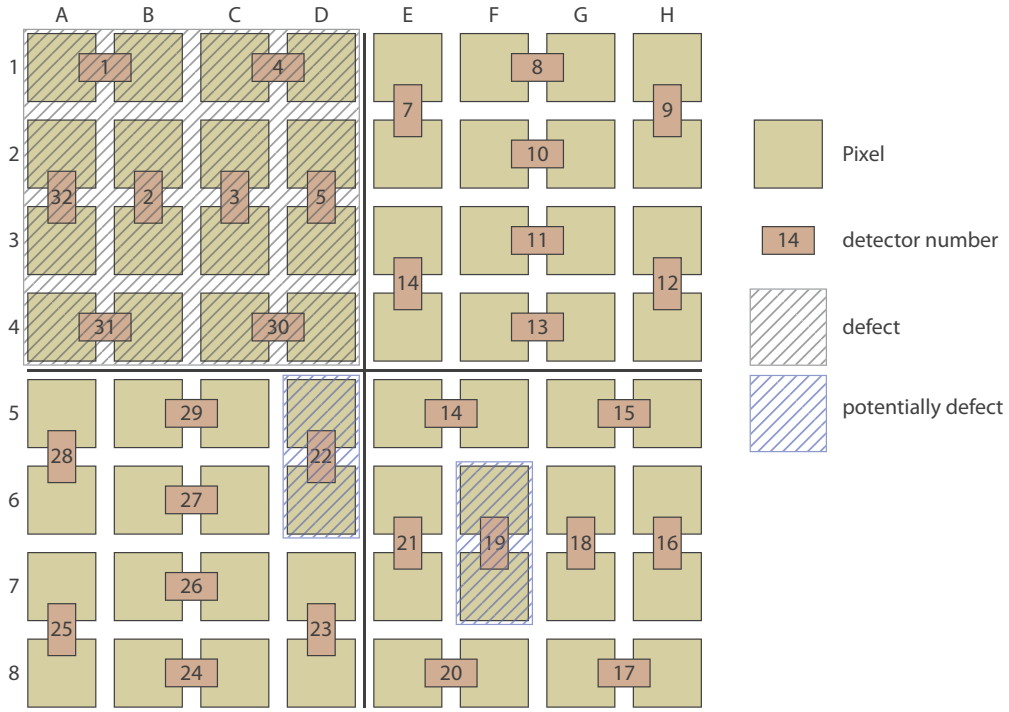

Fig. 4.3: Schematic of the detector in state when it was handed to ISOLDE for implantation. The first quadrant has interrupted field lines and thus no persistent current can be prepared. Detector 19 and 22 showed potential defects on the read-out lines in a visible inspection and are potentially broken.

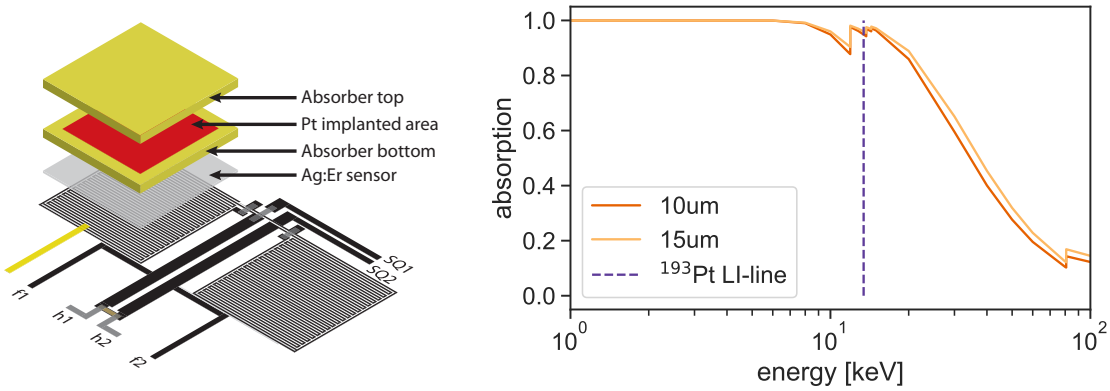

Fig. 4.4: Left: Schematic of a MMC detector, which is set up for an calorimetric measurement of an EC decay, in this case of ^{193}Pt. The absorber is situated on top the sensor, which made from Ag:Er. The sensor itself is fabricated in two steps: First a bottom layer is fabricated, which then is implanted with the source material. After that a second absorber layer is put on top to enclose the source within the absorber. Right: Photon absorption of the setup calculated for different thicknesses of the upper absorber. The bottom absorber was fixed to 7 µm, since this can not be changed anymore. The LI line of ^{193}Pt is indicated, since this is the most energetic main resonance of this isotope. It is clearly visible, that the photon loss is mostly dominated by the thin bottom absorber, so that a thicker top absorber of 15 µm does not come with a real advantage over a top absorber of 10 µm.

with a light microscope, weighing of several absorbers and the quotient of absorption coefficients for two different x-ray lines. The knowledge of this thickness is essential to estimate the quality of source enclosing.

4.2 Additional Absorber Layer

To enclose the source in a gold absorber, the absorber is fabricated in two steps: First, the whole detector with the bottom layer of the absorber is produced and after implantation, a second absorber layer is put on top of the first one to achieve a full 4π enclosure of the implanted atoms. This is shown in Figure 4.4 left. While implantation, as well as realization and fabrication of the second absorption layer will be explained in more detail in the next section, here the design decisions for this second absorption layer will be discussed.

The relaxation energy in an EC process is released in the form of Auger-electron and photons. The latter can origin either directly from dipole radiation of the daughter nuclide or from Bremsstrahlung of the released electrons. Such photons can have energies in a range of 10 keV and above. As a result they might escape the absorber,

depending on the absorber's exact geometry and material. This might not only unproportionally reduce the measured intensity of lines where the absorption efficiency is lower, but might also lead to a wrong attribution of decay events. For example in the case of ^{193}Pt if a $2s$ electron is captured, an electron from the $3p_{1/2}$ shell might relax into the generated core hole while emitting an x-ray photon. If now this x-ray photon escapes the absorber, only the energy released by the following relaxation of state with a core hole in the $3p_{1/2}$ shell will be measured: A $2s$ capture event (LI-line) would, after loss of the photon, appear as a $3p_{1/2}$ (MII-line) capture in the energy spectrum. So a bad source enclosure would not only reduce measured line intensities, but would also shuffle intensities from lines of high energy to matching lines of lower energy.

A higher stopping power for x-ray photons is simply achieved by increasing the thickness of the absorber. But since the corresponding increase in heat capacity lowers the achievable energy resolution, as was described in chapter 3, the thickness should be chosen just large enough to achieve a good enclosure. For the detector at hand it was not possible to adjust the thickness of the lower absorber to the experimental purpose, since it was already fabricated. With its estimated thickness of 7 µm it is rather thin for the energies up to about 14 keV of the main ^{193}Pt resonances. Figure 4.4 right displays two calculations of absorption efficiency for x-rays for different thicknesses of the upper absorber, which still can be adjusted. As expected there is not a large difference between an upper absorber thickness of 10 µm or 15 µm, since the lower absorber dominates in both cases the photon loss. But it is also indicated that for all energies up to the LI line, the photon loss is below 15%. Since the branching ratio of photons even in the LI line is expected to be below 5%, this would result in a photon loss on the per mil level. Hence the thickness of the upper absorber is chosen to 10 µm to achieve a better energy resolution and still have a small safety margin if the absorber turns out smaller then expected during fabrication.

4.3 Implantation and Post Processing

The fabrication of the implantation mask, as well as of the second absorber layer was done on the basis of photolithography in the internal cleanroom facility of the Kirchhoff-Institute for Physics. In general, photolithography utilizes photosensitive chemicals called photoresists (also abbreviated to resist in the following). Such a resist is evenly distributed over the substrate that is supposed to be structured by spin-coating. Then, a geometric pattern is transferred into the resist via an optical method such as aligned photomasks or mask-less LASER alignment and subsequent exposure of the resist to a matching chemical called the developer. This geometric pattern in

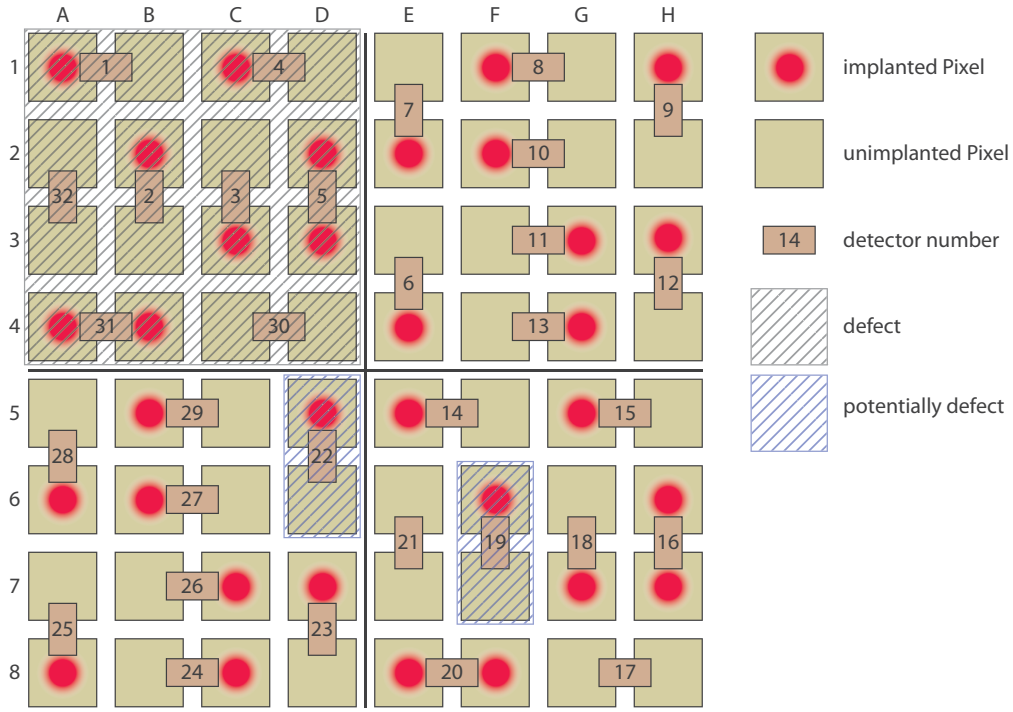

Fig. 4.5: Schematic of the detector and its implantation. Red dots indicate the pixels where ^{193}Pt was implanted and a second absorber layer is necessary to enclose the source.

the resist then allows to remove (i.e. via etching) or add (i.e. via electroplating or a so-called lift-off process) material in the structured pattern.

Implantation

Figure 4.5 shows which pixels were implanted. This was done by covering the chip with photoresist and structuring the area to be implanted with photolithography as explained above. While each pixel is a square of 500 µm x 500 µm, the implanted area is a square of 470 µm x 470 µm. This ensures a good source enclosure even with some misalignment. Since all of this is done with a single chip, a misalignment of several µm is possible. This is due to the lack of precise alignment structures and border effects of the resist. Those border effects result from the topography of the photoresist, which is not planar near high edges and causes refraction of the light used to expose the photoresist.

The prepared chip then was sent to ISOLDE for implantation. There ^{193}Pt was implanted in 32 absorbers of the chip using on-line isotope mass separation. The chip was then let rested for a few months, to allow short-lived isotopes that might have been accidentally implanted together with the ^{193}Pt to decay away.

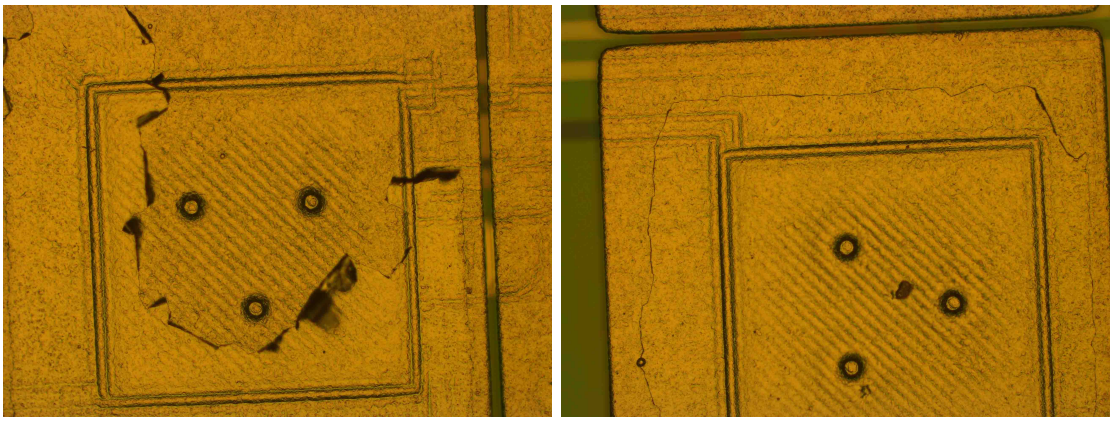

Fig. 4.6: Left: A picture of a pixel where the protection layer came partially of. Pieces of the detached gold foil sticking upwards are clearly visible. Right: A pixel where the protection layer mostly stayed on. Only the rough edges indicate that a minor amount of material was removed.

Post Processing

Protection layer and cleaning: The first step after receiving the implanted chip, still with the implantation mask on, was to sputter deposit a thin (100 nm) layer of gold on top as a protection layer. Commonly the substrate is cleaned beforehand by ion cleaning to remove water and other adsorbents on top of the target area. Those could lead to a bad adhesion of the deposited material. This step had to be omitted for this protection layer since it would have also removes several nm of gold, which is also roughly the penetration depth of the implanted ions. This cleaning process would actually remove most of the source material and could drop the activity within the absorber up to several orders of magnitude. After the deposition of the protection layer, the resist was removed using solvents such as DMF (Dimethylformamide) and NMP (N-Methyl-2-pyrrolidone) and ultrasound cleaning. Additionally some residues on the bond pads had to be removed manually. During the necessary ultrasound cleaning the implanted Pixel H3 belonging to detector 12 of the array came off.

Partial loss of the protection layer: Since the ion cleaning had to be omitted for depositing the protection layer, the layer actually detached at least partially on several pixels. Figure 4.6 shows an example of this on the left-hand side while showing a counter example of a well attached protection layer next to it on the right. This meant, that to proceed with the second absorber layer, one had to either omit the ion cleaning again or use ion cleaning and remove the source in the unprotected areas. Since omitting the ion cleaning could result in the whole absorber layer detaching, which could render the whole detector inoperative, it was decided to use some ion cleaning, even if this meant a reduction of the ^{193}Pt activity.

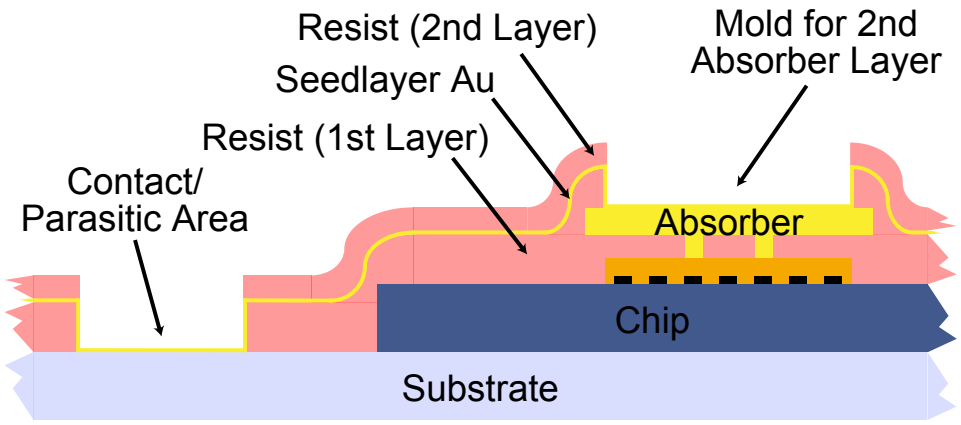

Fig. 4.7: Schematic of the multiple layers that are applied to before the second absorber layer can be electroplated. A first layer of resist ist structured in a way that all areas of the chip are protected except for the 480 µm x 480 µm large squares for the second absorber layer. Then a seed layer of gold is sputtered in such a way, that an electric contact can be ensured across all relevant edges. The a second layer of resist forms again the molds where later gold shall be electroplated.

Fabrication of second absorber layer: For the fabrication of the second absorber layer with a thickness of 10 µm a new multi-step process was developed, that allows for the electroplating of structures on single chips. A schematic of the process is shown in Figure 4.7. First the chip is glued on a glass plate of 25 mm x 25 mm. This does not only make the chip easier to handle, but is also later necessary to create a parasitic area and a contact for an electroplating step. Next, a first layer of resist is applied, with an estimated thickness of 10 µm. This resist layer also smooths out sharp edges, for example from the chip to the substrate and from the absorber to the chip. On this first resist layer, the mask for the second absorber layer is structured. The mask not only includes the area for the second absorber layer, which is 480 µm x 480 µm centered on top of each pixel which was implanted, but also a larger area on the glass plate as a parasisitic and contact area. In a next step a 100 nm layer of gold is sputter deposited followed by 200 nm layer, which is sputtered at an angle. This ensures an electrically conducting contact over edges of the photoresist, since also vertical surfaces are covered. This gold layer is the so-called seed layer and serves to create the electric contact to all areas where gold will later be electroplated to form the next absorber layer. As a last step before the electroplating, a second layer of resist is applied and again structured with the mask for second absorber layer and parasitic area on the glass plate. This parasitic area has a total size of 73 mm^2, which

is about tenfold the area of all 32 second-layer absorbers (total area of 7.4 mm^2). This ensures that the area is on one hand well defined and small unknown surfaces, such as the contact needle do not affect the total area in a relevant way. On the other hand it allows for the usage of larger currents (0.8 mA) for electroplating, while still keeping the growth rate low enough that the process runs within its well established parameters. Further the electroplated parasitic area can later be weighed to estimate the thickness of the electroplated gold layer and with that of the second absorber layer. It also is a large area at the edge of the substrate where the contact needle for the galvanisation is placed. After the electroplating the photoresist is lifted using again solvents and ultrasound. This also shatters the seed layer, so that the contact between the pixels is removed.

The final result can be seen on the right in Figure 4.8, next to the state after implantation on the left. The black dots and erratic lines on the second absorber layer are actually effects of protruding pieces of the protection layer as could be seen left in Figure 4.6 left. As a result the electroplated gold area is not even but still shows those protrusions, which appear black due to no light being reflected back to the optics of the microscope. In the whole process one pixel (H3) disconnected which renders the corresponding detector inoperable (detector 12). This happened during the initial cleaning in an ultrasound bath as mentioned above. The parasitic area weighted 15 mg, which results in a total thickness of approximately 11 µm (using a density of gold of 19.3 g/cm^3 and a total area of 71 $µm^2$, which is the parasitic area minus the area that was covered by the contact needle). This is close to the designed value of 10 µm.

4.4 Experiment Setup

First Stage SQUIDs

To select suitable front-end SQUIDs, several chips with in-house fabricated SQUIDs were tested and characterized. In the end six chips, with four SQUIDs each of the ASYM V2 design from the wafer designated HDSQ11b-w3, were selected. They have a feedback sensitivity of 41.5 $µA/\Phi_0$ and a input sensitivity of 8.7 $µA/\Phi_0$.

Cryogenic Setup

The detector chip and the FE SQUID chips are glued on an already existing copper holder with matching printed circuit board (PCB) which were both designed for the *maXs30* detector. This is shown in Figure 4.9. The connection between read-out lines of the detectors and the input coils of the SQUIDs is done with ultrasonic bonding.

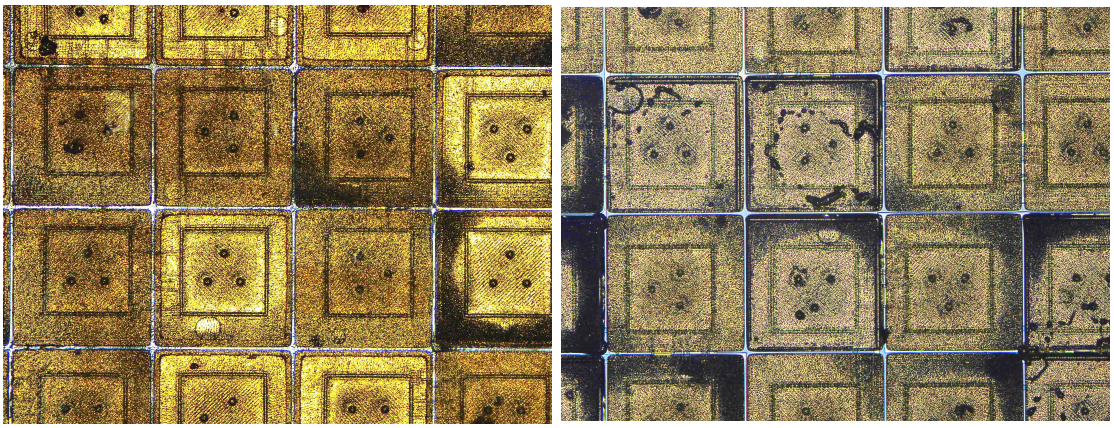

Fig. 4.8: Left: A picture of a part of the detector array still with the photoresist mask from implantation. The brighter areas are the implanted ones and free from resist Right: An area of the detector after the second absorber layer was successfully added. The second absorber layer appears slightly brighter and shows often with black dots and erratic lines. These are irregularities in the surface that result from the protruding pieces of protection layer that partially came of.

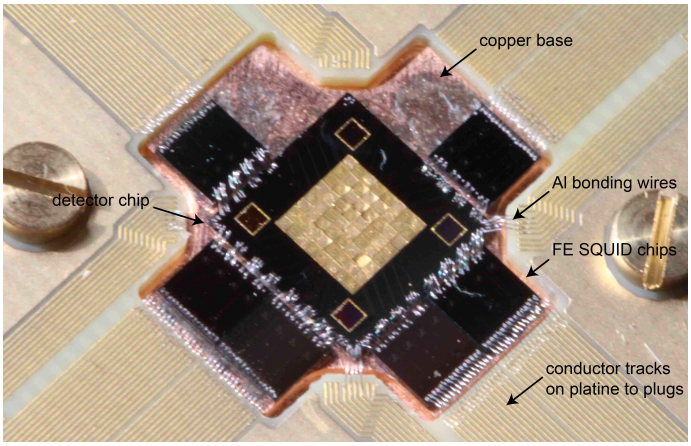

Fig. 4.9: The detector chip glued on the copper holder with six FE SQUID chips glued around it. The read-out lines of the detectors are connected to the input coils of the FE SQUIDs by Al bonding wires. The SQUIDs, as well as the lines to prepare the persistent currents are further bonded on conductor tracks on a printed circuit board. From there superconducting wiring leads to the SQUID amplifier arrays and outside the cryostat.

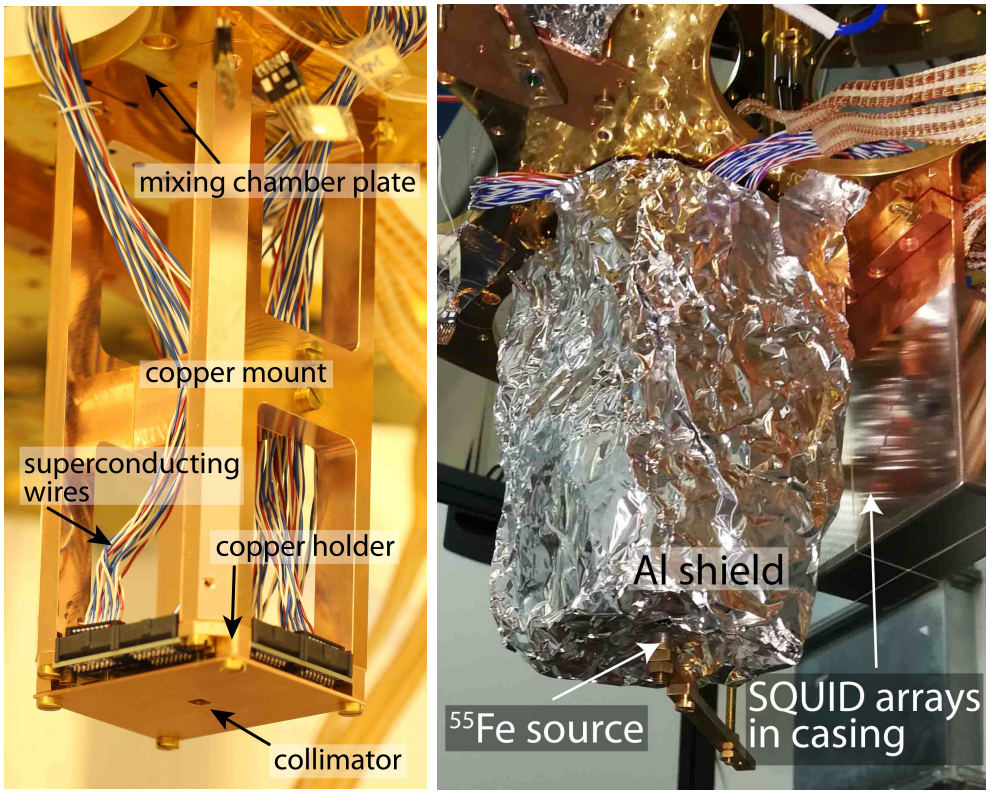

Fig. 4.10: Left: The copper holder with the added collimator placed on the designed copper mount, which is then mounted upside-down on the mixing chamber plate of the cryostat. The superconducting wiring leads from the circuit board to the SQUID amplifier arrays. Right: Those are mounted next to the setup. A superconducting shield made from aluminium encases the setup to shield it from external electromagnetic signals. An ^{55}Fe source is placed below the aluminium shield and in front of the collimator for energy calibration of the detector.

The bonding wire is 25 µm thick and made from Aluminium. The aluminium becomes superconducting at about 1.2 K, which is well above the operating temperature of the detector. To reduce the parasitic inductance introduced by these wires, two bonds are placed in parallel. Field- and heater-lines for preparing the persistent current, as well as current and voltage lines to the FE SQUIDs, are bonded on the conductor tracks of the PCB. From there superconducting wires lead outside the cryostat or to the amplifier SQUID arrays.

This copper holder is then connected on a copper mount. The copper mount, which can be seen on the left of Figure 4.10, was designed in the framework of this thesis to allow for the usage of the existing copper holder in the dilution cryostat which is used for the ECHo experiment. The mount is equipped with several possibilities to connect a shield, for example made from aluminium. For the measurements carried out in this thesis a provisional shield made from a thicker type of aluminium foil was

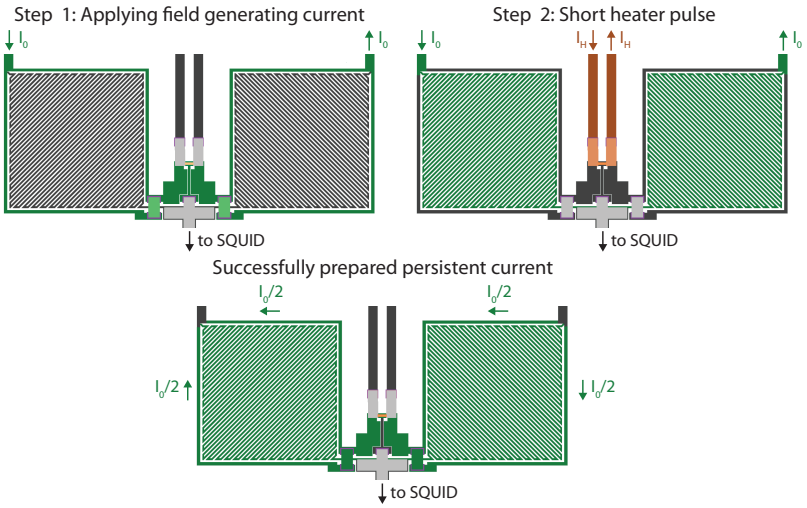

Fig. 4.11: The process of freezing in the persistent current which is needed to operate the MMCs. The bottom/top layer of niobium is depicted in dark/light grey. Bottom/top lines carrying currents are drawn in dark/light green. Lines carrying the heater current are drawn in dark/light orange. An overview over the different steps to prepare the persistent current is given in the text.

used, which is depicted in Figure 4.10 right.

Preparation of the Persistent Current

MMC detectors need an external magnetic field for polarizing the spins in the paramagnetic sensor, which is usually provided by a persistent current, as mentioned before. In case of the *maXs30* detector chip, this persistent current is prepared within all eight detectors of one quadrant of the chip at the same time using the following process, which is depicted in Figure 4.11. Step 1: The field current is provided via a current source connected to the field lines. Due to its comparatively lower inductance the current mainly flows through the box around the meanders. Step 2: A short heater pulse is applied to a resistor made from an alloy out of gold and palladium, which is situated on top of the so-called persistent current switch. There the niobium is locally heated above its critical temperature of 9.2 K, which opens the superconducting loop and forces the field current through the meander, which is the only remaining superconducting connection. Step 3: This short heater pulse the niobium cools down, and becomes again superconducting. Since the flux within this superconducting loop has to be conserved, the current within the meander now also remains when the current source providing the field current is switched of at last.

4.5 ^{55}Fe calibration source

In Figure 4.10 right, the ^{55}Fe source used for energy calibration is visible. ^{55}Fe decays under EC to ^{55}Mn. The spectrum is dominated by two main lines of ^{55}Mn K_α and K_β, which originate from vacancies in the 1s shell. Their energies are about 5.89 keV in case of the K_α, and 6.49 keV for the K_β line. Both lines have a complex substructure which is evaluated in depth for example in [Hol97]. An available ^{55}Fe source was chosen and mounted in such a distance, that the expected activity per pixel was 1 Bq.

5. Experimental Results

The detector together with the experimental setup was mounted in a dilution cryostat to be operated at mK temperatures. Using the available wiring in the cryostat, 11 of the 23 potentially working detectors on the chip were connected. They were evenly distributed over all three working quadrants. Several measurements were performed: First, a noise analysis was carried out, from which the status and quality of the single detector could be inferred. Then, data was acquired over a time of several days, with the aim to measure the ^{193}Pt activity and to acquire the energy spectrum of its EC decay. Those measurements were performed between April 24 and April 29 of this year. The total acquisition time for the data evaluated for the spectrum was approximately 107 h.

5.1 Chip Characterization and Noise Measurement

Overview and Qualitative Analysis

In all of the 11 available read out channels (each connected to one detector on the chip) the front-end SQUIDs functioned as expected and tested earlier. When preparing the persistent current using the procedure described in section 4.4, in two of the three quadrants the possible persistent current, which could be frozen in, matched the values achieved in earlier test before implantation. In quadrant 3 the possible field current of 30 mA was significantly lower than the earlier measured value of 60 mA.

In 10 of the 11 connected channels pulses generated by the absorption of x-rays emitted by the ^{55}Fe calibration source were observed after the persistent current was frozen in. In all 10 cases pulses for both polarity were observed. Only detector 13 did not show any pulses. A possible reason could be a broken connection to SQUID or an unknown damage to the detector itself.

After the detector chip was checked on its basic functionality, a noise measurement was performed on all channels using the in-house acquiring software developed in [Hen17]. Figure 5.1 shows an example of such a noise measurement for channel 14. As expected the noise shows a $1/f$ component which dominates lower frequency domains and plateaus at around 10 kHz, where it is dominated by the white noise which results from the two-stage SQUID read-out. The low pass behaviour at around 500 kHz is a result of the gain bandwidth product (GBP) of the room temperature amplifier.

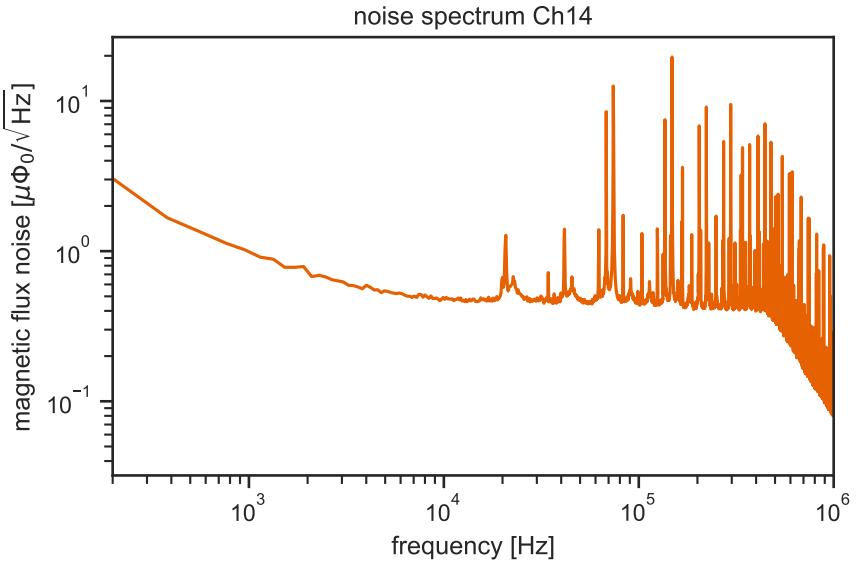

Fig. 5.1: An exemplary noise spectrum, here for channel 14. The plateau at higher frequencies is dominated by the intrinsic white SQUID noise of the front-end SQUIDs as described in section 3.2. The origin of the comb like noise structure on top, which starts at about 20 kHz is still under investigation.

In addition to this expected behaviour, a comb like noise structure appears above 20 kHz. This structure was visible in all channels and only differed in magnitude. In general the noise spectra of all channels were rather similar, with a maximum variation of up to a factor of 2 in the level of the white noise, which is caused by the different performances of the amplification SQUID arrays.

Electromagnet noise on the same frequencies as the unknown comb structure could be observed in the air of the lab by using a simple coil and a network analyzer. Still it is unlikely that this noise coupling into some part of the read-out chain causes the frequency comb. This is mainly due to two reasons: First, while some signal is visible in the air in the lab on the same frequencies, a lot of different, sometimes even stronger signals were present in the same frequency domain, but those were not visible in the noise measurement. Secondly, the noise was not only observed in the described setup, but also in two other experiments, which were also operated in the cryostat at the same time. The three experiments had substantially different ways of shielding for external electromagnetic waves, but also they had different read-out wiring. Still there was no major difference in the magnitude of the noise in the respective setups. The origin of the comb structure could not be fully understood within the time of the experiment end. The current presumption is, that the noise might have been introduced via the protective ground connection.

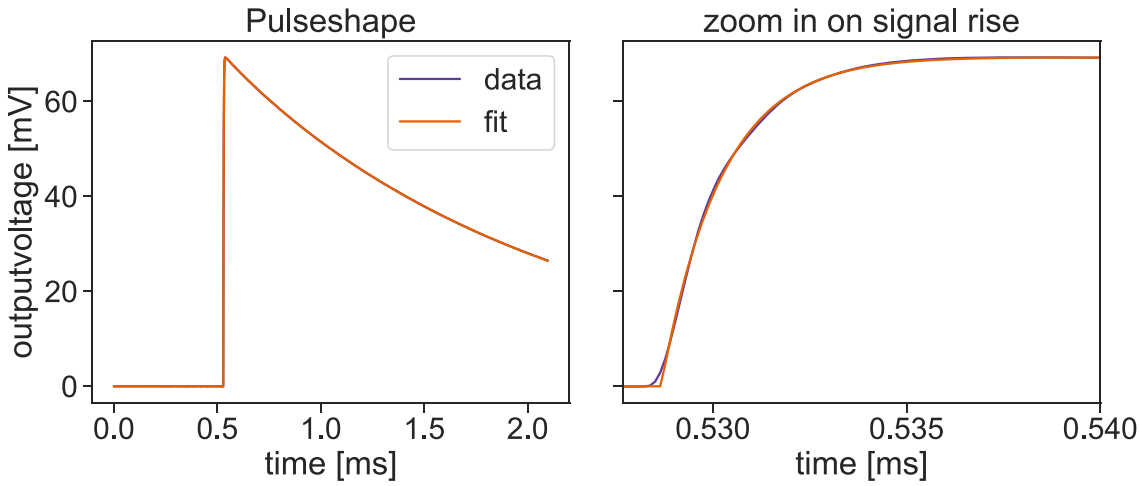

Fig. 5.2: Left: Template Pulse for the implanted pixel of Channel 14 and a fit of Equation 5.1. Right: Zoom in on the rise of the signal, which is on the timescale of µs compared to the ms timescale of the decay.

5.2 Pulse Shape Analysis

A detailed pulse shape analysis was performed in order to study the thermodynamic properties of pixels with implanted ^{193}Pt and second absorber layer in comparison to those with only the first layer of the absorber. For each pixel, multiple pulses of the K_α line from the ^{55}Fe source were averaged to increase the signal to noise ratio for this analysis. This so called template pulse is also later used for fitting each individual pulse. Typically the pulse shape is characterized by an amplitude A_0, an exponential rise with characteristic rise-time τ_r, followed by a decay with decay-time τ_d. Additionally a time offset t_0 is needed for fitting the pulses, but this does not change only the position in time, not the shape of the pulse. Using those parameters, the pulse shape is described by the following equation:

$$A(t) = \Theta(t - t_0) A_0 \left(e^{-(t-t_0)/\tau_r} - e^{-(t-t_0)/\tau_d} \right) \tag{5.1}$$

Figure 5.2 shows such the template pulse for the implanted pixel of channel 14 and a fit of the above description of the pulse shape, which describes the overall shape quite well. Such fits were performed for multiple pixels distributed over all three working quadrants.

The amplitude A_0 of a signal corresponding to a fixed energy corresponds to the change in temperature of sensor and absorber and thus also on the heat capacity of the absorber, according to Equation 3.4. A higher heat capacity of the absorber leads to a smaller signal amplitude. This could indeed be observed. For example the implanted pixel in detector 14 showed a signal amplitude of 69.8 mV for photons of

the K_α line, while the not implanted pixel of the same detector which does not have a second absorber layer showed an amplitude of 100.7 mV.

Further the rise times τ_r should also differ for different absorber thicknesses. The rise time of the *maXs30* detectors is slowed down in respect to the electron-spin-coupling by introducing a thermal bottleneck via islands and stems where the absorber rests on top of the sensor. The dominating factor is the heat flow from the absorber to the sensor which governs how fast the temperature and the magnetization of the Ag:Er sensor and thus the output voltage changes. The rise time is then given by the heat capacity of absorber C_A and sensor C_S, as well as the thermal conductivity G between them:

$$\tau_r = \frac{C_A C_S}{G(C_A + C_S)} \tag{5.2}$$

According to this equation, a higher values for C_S should also lead to a slower signal rise time. This is again observed and for the above example of channel 14, the implanted pixel shows a rise time of 1.55 µs, while the unimplanted pixel shows a faster rise time of 1.00 µs.

Quantitative Analysis of Temperature and Persistent Current

For a more quantitative analysis of the pulse shape the value of the thermal conductivity between sensor and absorber G can be calculated according to the Wiedemann-Franz law for a given temperature T and n connections with a cross section of A and a length of l:

$$G = \frac{\mathcal{L}\,T}{\rho_{Ag:Er}}\, n\, \frac{A}{l} \tag{5.3}$$

here $\mathcal{L} = 2.44 \times 10^{-8}\,\mathrm{W\Omega/K^2}$ is the Lorenz number and $\rho_{Ag:Er}$ the electric resistivity of Ag:Er. The latter depends mostly on temperature and the electric resistivity of silver at room temperature $\rho^{300K}_{Ag:Er}$, as well as its residual resistivity ratio RRR, but at low temperatures also on the erbium concentration c:

$$\rho_{Ag:Er} = \frac{\rho^{300K}_{Ag:Er}}{RRR - 1} + c\,6.76 \times 10^{-6}\,\Omega\,\mathrm{m} \tag{5.4}$$

Further the thermal dependencies of the heat capacities of absorber and sensor are relevant. While the the heat capacity of the absorber (with volume V) at these temperatures is simply given by the electronic contribution $C_A = \gamma\,T\,V$, the heat capacity of the sensor is additionally governed by the more complex thermodynamics of the spin-system. This means, that it also depends on external magnetic field and thus on the persistent current. To make quantitative predictions of this complex

Tab. 5.1: List of different pixel for which a full pulse shape analysis was performed. For the measured amplitude and rise times the best matching values for temperature and persistent current are given.

channel	polarity	implanted	temperature	persistent current
9	-	no	35 mK	7 mA
9	+	yes	35 mK	12 mA
11	-	yes	35 mK	8 mA
11	+	no	30 mK	8 mA
14	-	no	55 mK	35 mA
14	+	yes	50 mK	35 mA
25	-	no	45 mK	30 mA
25	+	yes	45 mK	20 mA

system, all further calculations are done by numerical interpolation of simulation data. This is especially true for calculations of the pulse height, where also the change of magnetization in the sensor is relevant, which again depends on temperature and persistent current.

For several channels corresponding pulse amplitudes and rise times were calculated for given arrays of different temperatures and persistent currents. Those were compared to the measured values for each of those pixels to find a best estimate for persistent current and temperature. The results from this analysis are listed in Table 5.1. Those results depend on values like the erbium concentration within the sensor or the thickness of the absorber, both of which are only known with a precission of about 10%. From a sensitivity analysis, a uncertainty of approximately 5 mK on the temperature and probably up to 5 mA on the persistent current is likely. The different values for the persistent current are not surprising, since the the pixels are distributed over different quadrants where different currents were frozen in. Within one detector, and in the case of detector 9 and 11 within one quadrant, the resulting currents are rather similar. This is slightly different for the temperature, where there is no apparent reason, why a temperature gradient of several mK should occur on the chip. Since it seems unlikely that this distribution of temperatures correctly represents the actual temperature on the chip, it is most likely either a result of an imprecise method or of slightly different behaviour of the detectors, which might be caused by imperfections in the fabrication process. But as a best estimate, an average temperature of about 40 mK can be taken.

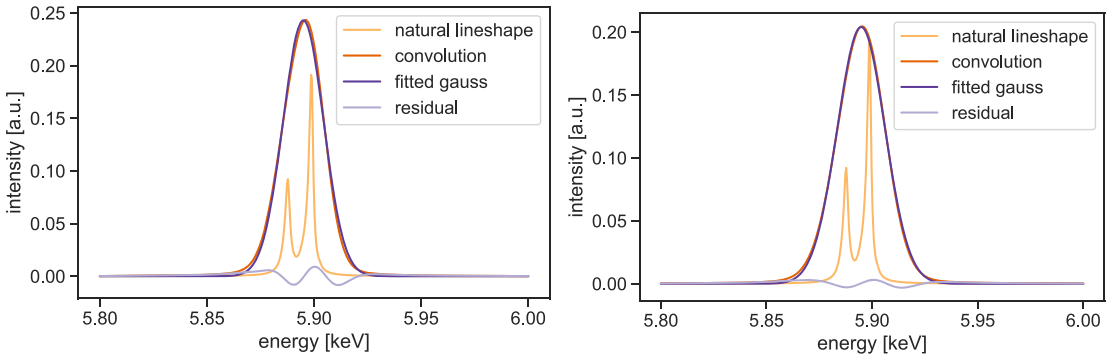

Fig. 5.3: Right: The K_α line of the ^{55}Fe calibration source with its natural line width in comparison to a convolution with a 16 eV (FWHM) Gaussian and a fitted Gaussian and the residue between the latter two. Right: The same for a convolution with a Gaussian with about 21 eV FWHM.

Expected Energy Resolution and Implications on Spectral Shape

The estimated detector temperature of 40 mK is significantly above the optimal working temperature of the detector which is (depending on the exact configuration, like absorber thickness and field current) in the range of 10-20 mK. This results in a lower signal amplitude and therefore in a lower energy resolution. For example, for a temperature of 40 mK and a field current of about 30 mA the expected energy resolution (FWHM) is 16 eV for an unimplanted and 24 eV for an implanted pixel. This is far from the sub 10 eV energy resolution the detector is capable of.

As a result of this, more intricate substructures can not be resolved. This is analyzed at the example of the K_α line of the ^{55}Fe calibration source. While it has a complex substructure, which is described in detail in [Hol97], with a detector resolution of 16 eV this substructure is not visible anymore, especially not to the naked eye as can be seen in Figure 5.3 left. Even the difference between a fitted Gaussian and the convolution is a minor shift of the peak energy to lower values and small difference. For the purpose of later energy calibration, the apparent value will be used. One important difference lays in the FWHM of the fitted Gaussian and of the Gaussian which is convoluted with the natural line shape: If the shape of the K_α line as it appears in a detector with an energy resolution of 16 eV (FWHM) is fitted with a simple Gaussian, the apparent energy resolution derived from this Gaussian is about 22 eV. As it is visible in Figure 5.3 right, for a worse energy resolution of about 21 eV the differences become even smaller. Here, the apparent energy resolution would be about 27 eV. As will be described in the next section for the purpose of data analysis all lines will be just fitted with Gaussians. Due to the low energy resolution this results in only minor trade-offs which are neglectable compared to the other challenges the evaluation process faced, while improving on robustness and

computation time of the used algorithms.

5.3 Measurement of the ^{193}Pt EC Spectrum

Data Analysis Concept

The analysed pulse time traces are acquired in a time frame of 2 ms with the pulse starting at 0.5 ms. This first quarter of the pulse, the so-called pre-trigger, is the current baseline of the detector and can differ from zero since the acquisition setup is DC coupled to the SQUID readout. The core concept of the utilized data analysis is the template fit method: For each pixel a template pulse of one of the main spectral lines is generated by averaging over a large number of signal traces. In this case the K_α was chosen, since it is the most intense one. This template pulse is the average of many pulses of this particular energy range. To fit now the individual pulses, the template pulse is simply offseted by a constant and scaled with a scaling amplitude. The scaling value is saved as the amplitude of that particular pulse. Quality control parameters as for example the summed squares of the fit residuals χ^2, the χ^2 for the so called pre-trigger, which is the part before the signal rise, or a rate between amplitude and integrated area under the pulse called ζ are also saved.

Now noise, for example caused by cell phones, or events like pile-ups, where a second energy input occured before the detector signal decayed back to its ground state, are filtered by introducing cuts on the above mentioned quality parameters.

Pre-trigger Offset

One important parameter to mention is the so-called pre-trigger offset or just offset of the signal. It is the voltage offset of the whole signal, which can change due to temperature fluctuations on the chip that slightly alter the output voltage, due to the detectors being not perfectly gradiometric as described in section 3.1. This can be used as an alternative parameter for correcting for temperature drifts which also slightly alter the pulse height for events of the same energy. Ideally, a special non-gradiometric pixel, a so called temperature pixel, is used for this, but on the used detector chip, the only temperature pixel is situated on the broken quadrant 1. Because of this, the temperature correction was performed using the pre-trigger offset as a temperature proxy.

Apart from the temperature influence on the pre-trigger offset, there seems to be another source of variability in the pre-trigger value. Figure 5.4 shows the pre-trigger values for all measured pulses in the implanted pixel of detector 14. While there are also continuous drifts which can be attributed to temperature fluctuations on

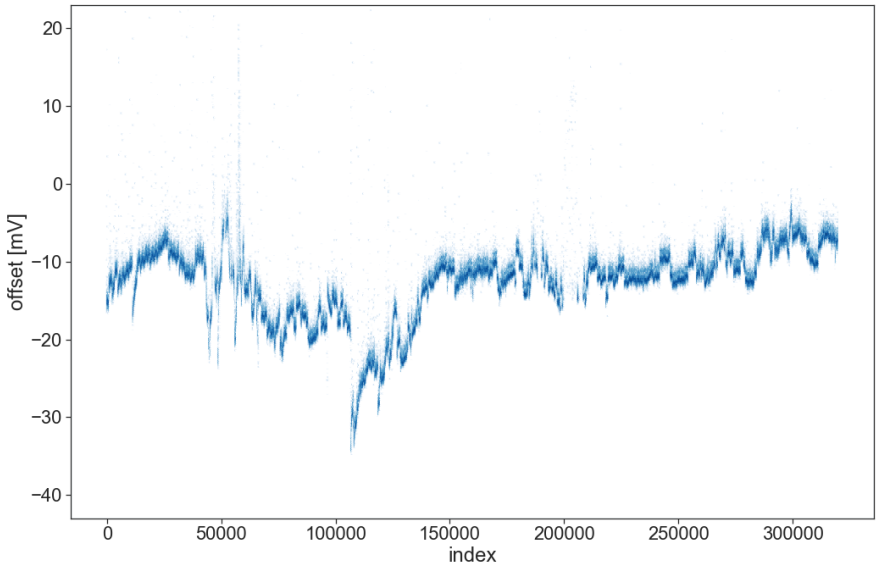

Fig. 5.4: Drift of the pre-trigger offset of the pulses. While a continuous drift is expected due to temperature fluctuations, there is no established explanation for the sudden jumps. They might be caused by a loss of magnetic fluxquanta in the meander.

the chip, there are also several sudden jumps occurring. Different working points of the SQUID can in principle explain sudden jumps of the pretrigger, but such jumps should have a magnitude of about 4 V for the used SQUID and electronics configuration. While the origin of these smaller jumps is at the moment unknown, it was observed that those jumps might come with slight gain changes of the detector. This means that groups that are separated by a offset jump should be temperature corrected and energy calibrated separately or the resulting energy resolution might be compromised. But this can only be done, if the total amount of events in such a subset is large enough for a reliable energy calibration. The analysis was carried out for a total of 23 groups, so called pre-trigger families, of pulses that seem to have a continuous pre-trigger value for the implanted pixel of channel 14, since this pixel showed the highest ^{193}Pt activity as will be shown later.

Energy Calibration

Each pre-trigger family is first temperature corrected against the offset as described above and then energy calibrated. In this case the K_α and K_β line of the ^{55}Fe calibration source were used. Each is fitted using a Gaussian profile and then these two points are used to calculate a calibration curve that matches pulse amplitude to energy. With the additional condition that of zero crossing a second order polynomial is used. All evaluated detectors showed a non-linearity of less than 1% at an energy

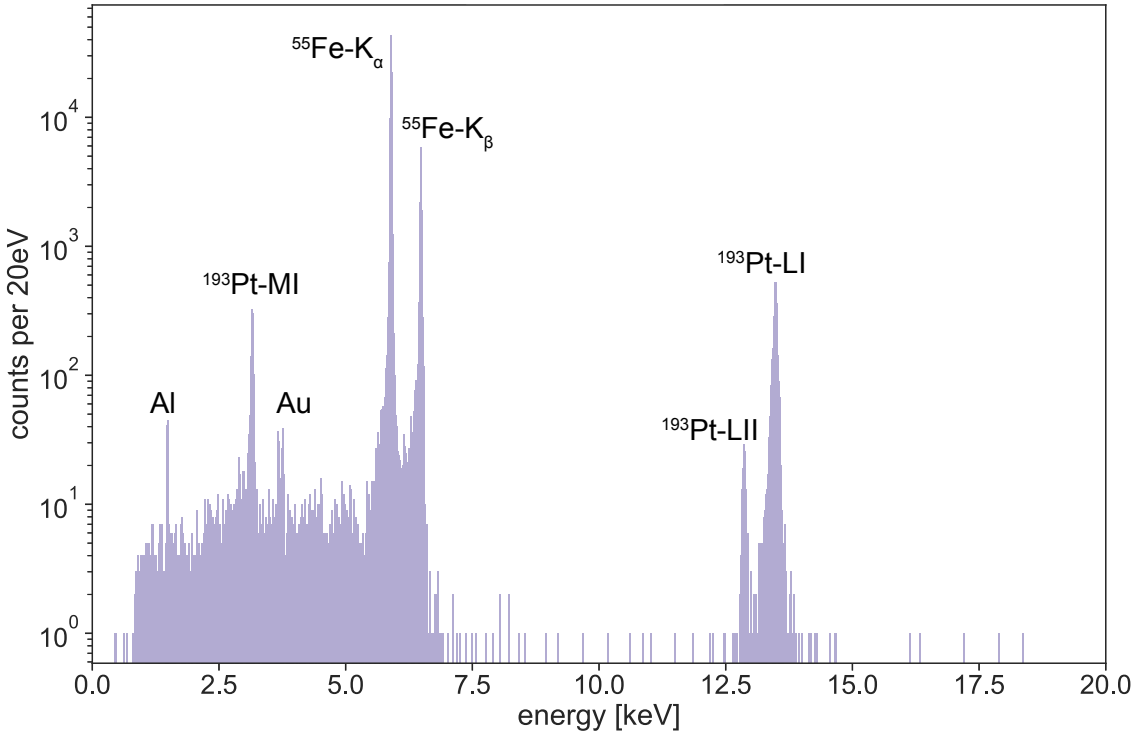

Fig. 5.5: Measured spectrum of the ^{193}Pt implanted pixel on detector 14. The two lines of the ^{55}Fe calibration source dominate the spectrum. In total three ^{193}Pt lines are visible. Additional Au and Al lines indirectly caused by the calibration source are also visible. All individual lines are further analyzed and explained in the text.

of 6 keV. This is in good agreement with earlier measurements with MMCs and also with other measurements of the same detector design [Hen17].

Measured Spectrum

The complete measured spectrum from the implanted pixel of detector 14 is shown in Figure 5.5. It consists of 69 290 detected pulses in the shown energy region, plus an additional 11 counts above 20 keV which are not shown in the spectrum. It is dominated by the ^{55}Fe calibration source with its K_α and K_β line at about 6 keV. In the energy range between 12 keV and 15 keV the LI and LII line of ^{193}Pt is visible. In the energy region below 6 keV is a plateau, likely caused by scattered photons of the K_α and K_β lines, for example via Compton scattering in the collimator, the aluminium shield or the source compound itself. This also explains why this background only exists below the two ^{55}Fe lines. The plateau abruptly disappears at around 1 keV, which is due to a high set trigger value in data acquisition software. The MI line of ^{193}Pt can be observed at an energy of about 3 keV. Three additional lines, one at about 1.5 keV and a double line at roughly 3.7 keV are visible. Those lines do also

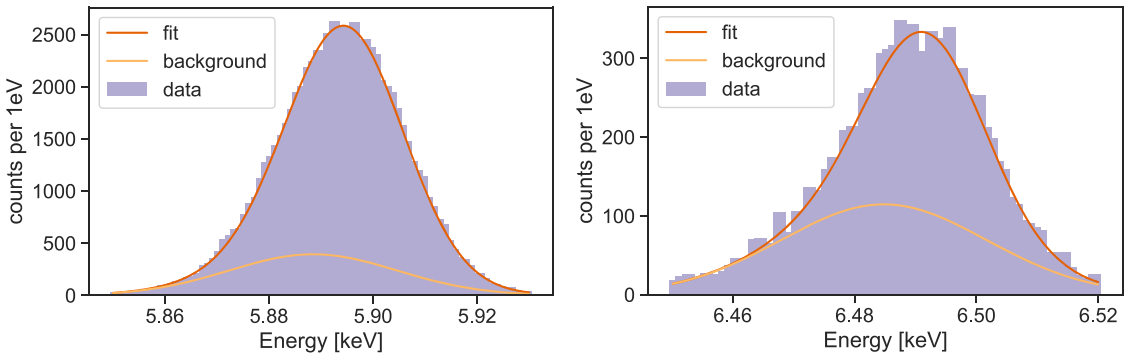

Fig. 5.6: Left:K_α line of ^{55}Fe, centered at 5894.7 eV with a FWHM of 26.0 eV. Right: K_β line of ^{55}Fe, centered at 6491.9 eV with a FWHM of 22.6 eV

appear in spectra of unimplanted pixels, which leads to the conclusion that they are most likely not the result of contaminant in the implantation process. In the following each of the lines will be discussed in detail.

The ^{55}Fe lines

The K_α and K_β line of the calibration source can be seen in Figure 5.6. A single Gaussian can not describe the observable lineshape. Introducing a second Gaussian results in a good fit to the measured data. This second Gaussian shows a slightly lower peak energy, bigger FWHM and a lower amplitude. It is likely, that pulses with different gain values resulting from imperfect pre-trigger separation make up this additional part of the signal. The K_α line is centered at 5894.7 eV with a FWHM of 26.0 eV. This apparent resolution of 26.0 eV corresponds to a real detector resolution of 21.0 eV as was described above. This energy resolution fits the expected energy resolution of 24 eV which was estimated for a temperature of 40 mK and a persistent current of 30 mA for an implanted pixel. The K_β line is centered at 6491.9 eV with a FWHM of 22.6 eV.

Al and Au-escape Lines

The first additional spectral line is centered at 1481 eV with a FWHM of 26 eV. This energy matches two known x-ray transitions in aluminium: The KL_2 and the KL_3 transition [Sch94]. Their expected values are 1487.1 eV and 1487.5 eV. This line is caused by de-excitation of aluminium atoms in the shield made from aluminium foil, which were excited by the ^{55}Fe calibration source. This also matches with the fact, that this line is also visible in unimplanted pixels.

The other two unknown lines, which can be seen in Figure 5.8, are centered at 3682 eV

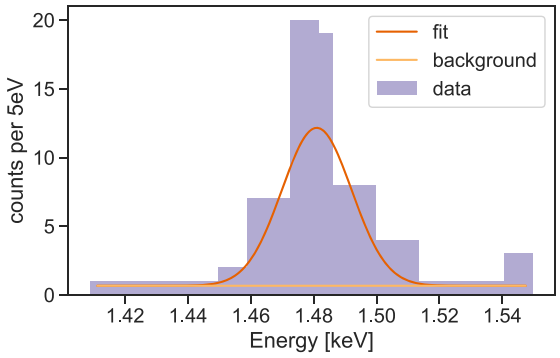

Fig. 5.7: Al KL_2/KL_3 transition, centered at 1481 eV with a FWHM of 26 eV

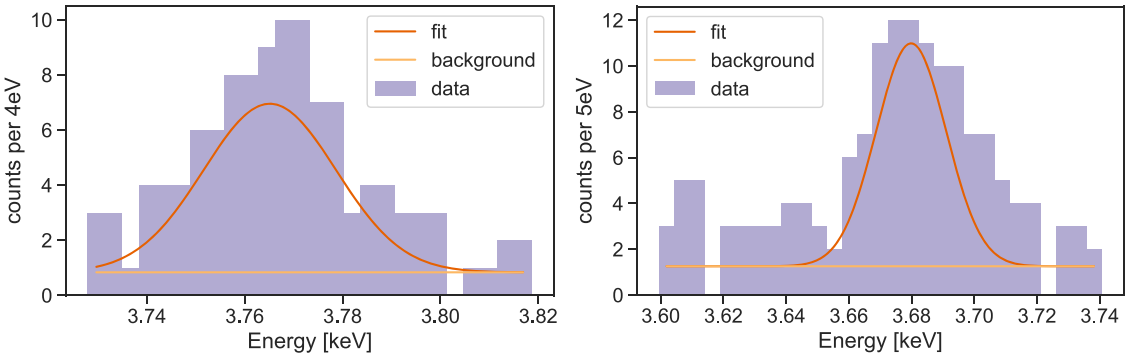

Fig. 5.8: Left: The first Au escape line, centered at 3682 eV with a FWHM of 35 eV. Right: The second Au escape line, centered at 3765 eV with a FWHM of 31 eV

and 3765 eV with a FWHM of 35 eV and 31 eV. These lines are so called escape lines of gold, as was already observed before [Lin07]: When a ^{55}Fe K_α photon is absorbed in one the gold absorber of the detector some of the energy E_{loss} can excite a gold atom. If now the de-excitation of this atom releases a photon there is a finite chance that it leaves the absorber, which then results in a signal of an apparent energy of $E(K_\alpha) - E_{\text{loss}}$. For a good source enclosure this only happens for external calibration sources, since there the energy input is already at the surface of the absorber and makes this process much more likely. In principle this process happens also for the K_β line, but since this is a higher order process and the K_β line is suppressed by about an order of magnitude compared to the K_α line, those escape lines are only observed for the latter one. The two observed gold escape lines result from M/N transitions with an energy of 2205 eV for the lower energy and 2123 eV and 2118 eV for the higher energy line. With a K_α energy of 5895 eV, the expected values for the escape lines are 3690 eV for the first and 3772 eV and 3777 eV for the second line. Again, this explanation fits to the fact that both lines are visible also in an unimplanted pixel.

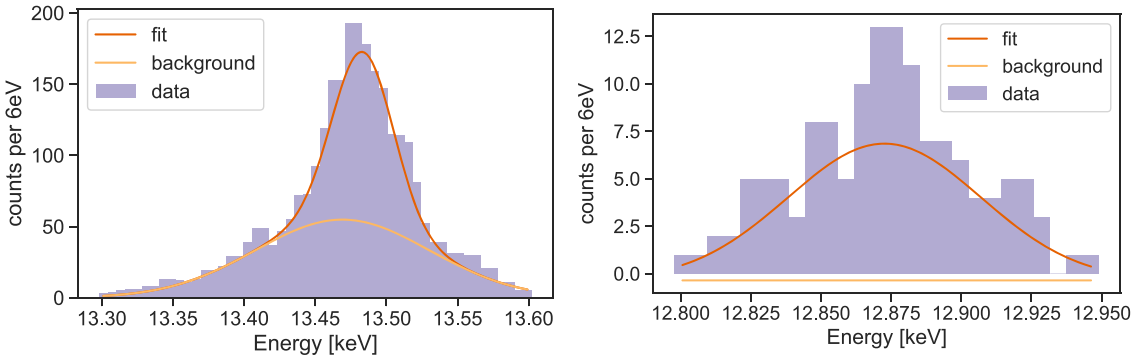

Fig. 5.9: Left: LI line of ^{193}Pt, centered at 13 483 eV with a FWHM of 50 eV. Right: LII line of ^{193}Pt, centered at 12 873 eV with a FWHM of 81 eV

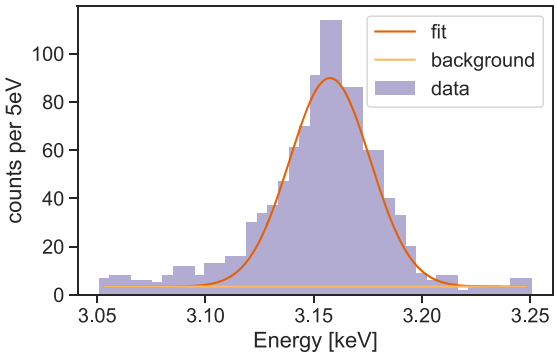

Fig. 5.10: MI line of ^{193}Pt, centered at 3158 eV with a FWHM of 44 eV

The ^{193}Pt lines

Three ^{193}Pt lines are clearly visible in the spectrum. The LI line (Figure 5.9 left) and the MI line (Figure 5.10) are again well described by Gaussian profiles. In case of the LI line again an additional Gaussian was used to describe the background. The LI line is centered at 13 483 eV with a FWHM of 50 eV, while the MI line is centered at 3158 eV with a FWHM of 44 eV. Remarkable is the higher FWHM compared to the ^{55}Fe lines. This is most likely caused by a imperfect energy calibration for the more than 20 pre-trigger families which were added up after energy calibration. This slight differences in calibration did lead to an additional broadening of the lines. The much less intense LII line (Figure 5.9 right) is centered at 12 873 eV with a FWHM of 81 eV. This bad resolution on the LII line should be the result of the low number of counts and thus high relative uncertainty on them. With a higher number of counts, the LII line should in principle show a similar profile as the LI line. In Table 5.2 the peak energies of the three lines are compared with values from atom physics and with the preliminary *ab-initio* calculation by Martin Brass. It is notable, that the measured values for the L-lines are higher than both the atomic literature value and

Tab. 5.2: List of the measured ^{193}Pt lines and there energies E_{exp} and FWHM in comparison to the literature values for the corresponding iridium atomic resonances E_{Lit} and the preliminary *ab-inito* calculation E_{ai} shown in Figure 2.5.

spectral line	E_{exp}	FWHM	E_{Lit}	E_{ai}
LI	13 483 eV	50 eV	13 423 eV	13 391 eV
LII	12 873 eV	81 eV	12 829 eV	12 781 eV
MI	3158 eV	44 eV	3176 eV	3138 eV

Tab. 5.3: List of implanted pixels, where a statistical significant number of counts was measured in region of the L-lines of ^{193}Pt. For each the number of counts in this energy range, as well as the resulting ^{193}Pt activity with statistical uncertainty is given.

pixel	polarity	counts in L-lines	^{193}Pt activity
11	-	105	0.41(4) mBq
14	+	8828	34.60(37) mBq
16	-	1672	6.55(16) mBq
16	+	1806	7.08(17) mBq
18	+	2379	9.32(19) mBq
26	-	692	2.71(10) mBq
27	-	309	1.21(7) mBq

the theoretical prediction, while the measured energy for the MI line is lower than value from atomic literature but by the same amount higher than the theoretical prediction.

Activity Analysis

Finally, an activity analysis of all measured detectors was carried out. For this a spectrum was evaluated for all individual pixels. This was done without a thorough separation of pre-trigger families, since a rough energy calibration is enough to extract the total number of counts in a line. For each pixel the number of counts in the energy region of the ^{193}Pt L-lines is taken. Then an additional factor of 1.5 was applied, to take the spectral weight of the L-lines into account, which is about 66% of the complete spectrum. Together with the total acquisition time of 107.37 h an activity for ^{193}Pt in each pixel was calculated.

Further the count rate of the ^{55}Fe source was calculated in a similar way, by taking the number of events in the energy range of the K_α and K_β lines and dividing that by the total measurement time. The rate was mostly in the range of 0.71-0.75 Bq which

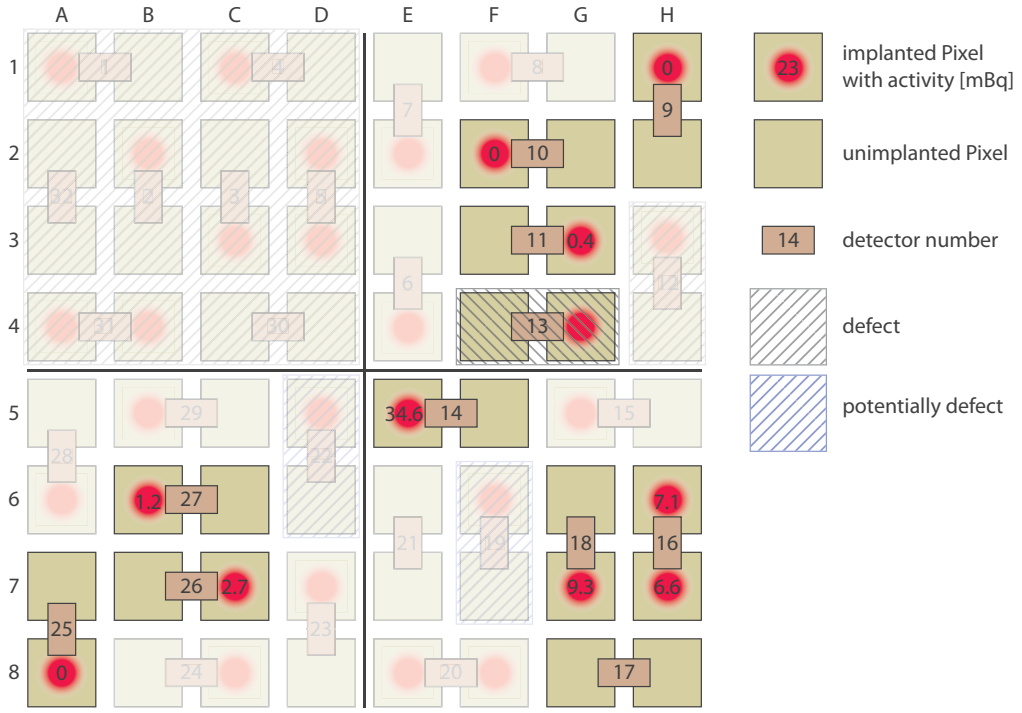

Fig. 5.11: Schematic of the chip, with not measured detectors faded out. In all implanted pixels the measured ^{193}Pt activity is noted in mBq. In detector 13 the activity could not be estimated, since the detector did not function.

fits the expected value of about 1 Bq. Only a few pixel showed lower rates down to 0.29 Bq, but up on further inspection it turns out that all of them are located at the edge of the collimator and are most likely partially hidden.

The ^{193}Pt activity for all pixels which showed a statistical significant increase in counts in the L-line region is given in Table 5.3. Further, a schematic with all measured pixels and activities for the implanted pixels can be found in Figure 5.11. The maximal measure activity of 34.6(4) mBq substantially lower than the aimed for value of 1 Bq, with some pixel showing activities of less than 1 mBq. The spread in activity can be explained by the partial loss of the Au protection layer and following ion cleaning. On the other hand not all pixel were damaged (for example the implanted pixel of detector 14 which had an estimated coverage of over 90% and the general low activity might be due to an overestimation of the exposure during implantation.

At the same time the results achieved in this first characterization of the detector with implanted ^{193}Pt show that it can be used for high energy resolution measurements of the EC spectrum after improving the set up to reach low temperatures. In this case

While it is true that the protection layer sputtered directly on the implanted area did not stick well, for several pixel a covered area of more than 90% was observed. A removal of the implanted atoms during the ion cleaning process which was performed before sputtering the seed layer for the second absorber layer can not explain the low activities. This leads to the assumption that either an error occurred during the implantation process itself or a major part of the implanted atoms was lost even before the protection layer could be sputtered on top.

6. Summary and Outlook

The analysis of the electron capture spectrum of ^{163}Ho is a promising tool to investigate the effective mass of the electron neutrino. A well established theoretical description of such a spectrum is indispensable to allow for trustworthy results. Measurements of high energy resolution and low background ^{163}Ho EC spectra have shown structures which are not described by the simple theory proposed in [DR82] These unforeseen structures represent a few percent of the total number of counts. The discrepancy between data and theory has a large effect on the size of the systematic errors on information on the effective neutrino mass extracted from analysis of the end point region. Recently, a new *ab-initio* calculation provides a promising approach, but further developments and verification needs to be supported with experimental data on different nuclides that undergo EC. ^{193}Pt is one of the candidates to provide such results.

In this work a detector array of metallic magnetic calorimeters, with some absorbers enclosing ^{193}Pt at the ISOLDE/CERN facility, was completed by adding a second absorber layer to fully enclose the implanted source. This was done in order to perform a calorimetric measurement of the ^{193}Pt EC spectrum. In the in-house cleanroom facility, a process for adding this second absorber layer on the implanted pixels was developed. An experimental setup was complemented to allow for operation of the implanted detector in a dilution cryostat.

The detector performance in terms of signal shape an energy resolution was investigated. An analysis of signal amplitude and rise time showed the expected differences for absorbers with or without the second absorber layer. Further, the signal shape analysis indicated that the temperature on the chip during measurement was in the range of 40 mK, which is above the optimal operating temperature of about 20 mK.

The ^{193}Pt activity was measured for 10 of the implanted absorbers, by counting the number of events in the L-lines over the measured time. At a maximum of 34.60(37) mBq, the observed activities were more than an order of magnitude lower than the expected value of 1 Bq.

Finally the EC spectrum of ^{193}Pt was measured. An external ^{55}Fe source was used for energy calibration. The energy resolution of the implanted detector was 21 eV (FWHM) at an energy of 6 keV and an operating temperature of 40 mK. This energy resolution is worse then the results achieved with similar detectors, but close to the expected energy resolution for the estimated temperature of 40 mK. Therefore a lower detector temperature should lead to a better energy resolution.

Despite the low ^{193}Pt activity, the LI, LII and MI line of its EC spectrum were observed and characterized. Energy resolutions of about 50 eV for LI and MI line show that temperature correction and energy calibration for the individual evaluated data subsets is far from ideal and compromise the energy resolution. The measured Gaussian width of 81 eV (FWHM) for the LII line is most likely a result of low statistics.

Building on the results of this first characterization, several aspects have been identified where improvements are possible. A key problem is the low activity of the implanted ^{193}Pt source. While this can not be changed anymore, a targeted measurement of the most active detector can be carried out over a longer period of time, while using the other available wiring to check the still unmeasured detectors on the chip. This opens the possibility to still find detectors with a similar or greater ^{193}Pt activity. Further, to reduce the background-level for the lines with an energy below 6 keV, the x-ray rate of the calibration source can be adjusted down by an order of magnitude. This would reduce the intensity of the calibration lines to a level of the LI and MI lines of ^{193}Pt, while still allowing for a good energy calibration. The background plateau and the secondary lines (Al and Au escape) would be reduced by the same factor. In a subsequent measurement the calibration source could be completely omitted after the energies of the main lines are experimentally well established and can be used to calibrate the spectrum. An additional option would be to use a different calibration source that has more energy lines, spread over a wider energy range, as for example ^{241}Am. This would allow for a more precise calibration especially at higher energies, to better deduce the peak energies for example for the LI and LII line.

To improve on the energy resolution of the detector, the chip temperature has to decrease. This can be done by improving the thermal coupling between chip and copper setup and to the mixing chamber plate of the cryostat. Further, during the run the temperature of the mixing chamber plate fluctuated by several tenths of mK, while a stabilization about 100 times better was achieved with similar cryostats within our working group. Since the discussed detector chip is not equipped with a working temperature pixel, a better temperature stabilization of the mixing chamber platform temperature is necessary. A more stable temperature would dramatically reduce the problem arising from the sub-optimal method for temperature correction. It was also observed that a more stable temperature likely reduces the rate of pretrigger jumps, that cause the necessity to perform the data evaluation separately on small data subsets. Hence, a decreased rate of these jumps would allow to analyze larger data subsets and would increase the stability on the different steps of evaluation, due to a higher statistic. Last but not least, the expected improvement in energy resolution would allow for a more precise energy calibration, since sharper spectral

features allow for a more precise fit of the calibration lines to the measured data.

The results with the present performance, as well as the amount of possible improvements lead to the conclusion, that, with a number of targeted adjustments, considerable improvement on the knowledge of ^{193}Pt electron capture spectrum can be made with the current implanted MMC array.

Literaturverzeichnis

[Ahm02] Q Retal Ahmad, RC Allen, TC Andersen, JD Anglin, JC Barton, EW Beier, M Bercovitch, J Bigu, SD Biller, RA Black, et al., Direct evidence for neutrino flavor transformation from neutral-current interactions in the sudbury neutrino observatory, *Physical review letters*, **89**(1), 011301, 2002.

[Alv37] Luis W Alvarez, Nuclear k electron capture, *Physical Review*, **52**(2), 134, 1937.

[Bai83] PA Baisden, DH Sisson, S Niemeyer, B Hudson, CL Bennett, und RA Naumann, Measurement of the half-life of ho 163, *Physical Review C*, **28**(1), 337, 1983.

[Bra18] M Braß, C Enss, L Gastaldo, RJ Green, und MW Haverkort, Ab initio calculation of the calorimetric electron-capture spectrum of ho 163: Intra-atomic decay into bound states, *Physical Review C*, **97**(5), 054620, 2018.

[Bru82] J. J. P. Bruines, V. J. de Waal, und J. E. Mooij, Comment on: 'Dc SQUID: Noise and optimization' by Tesche and Clarke, *J. Low Temp. Phys.*, **46**(3), 383–386, 1982.

[Cam01] JL Campbell und Tibor Papp, Widths of the atomic k–n7 levels, *Atomic Data and Nuclear Data Tables*, **77**(1), 1–56, 2001.

[Cla04] J. Clarke und A. Braginski, *The SQUID Handbook: Fundamentals and Technology of SQUIDs and SQUID Systems*, volume 1, Wiley - Weinheim, 2004.

[Coh72] RL Cohen, GK Wertheim, A Rosencwaig, und HJ Guggenheim, Multiplet splitting of the 4 s and 5 s electrons of the rare earths, *Physical Review B*, **5**(3), 1037, 1972.

[Des03] Richard D Deslattes, Ernest G Kessler Jr, Paul Indelicato, L De Billy, E Lindroth, und J Anton, X-ray transition energies: new approach to a comprehensive evaluation, *Reviews of Modern Physics*, **75**(1), 35, 2003.

[DR82] Alvaro De Rújula und Maurizio Lusignoli, Calorimetric measurements of 163holmium decay as tools to determine the electron neutrino mass, *Physics Letters B*, **118**(4-6), 429–434, 1982.

[DR16] A De Rújula und M Lusignoli, The calorimetric spectrum of the electron-capture decay of 163 ho. the spectral endpoint region, *Journal of High Energy Physics*, **2016**(5), 15, 2016.

[Eli15] Sergey Eliseev, Klaus Blaum, M Block, S Chenmarev, H Dorrer, Ch E Düllmann, C Enss, PE Filianin, L Gastaldo, Mikhail Goncharov, et al., Direct measurement of the mass difference of ho 163 and dy 163 solves the q-value puzzle for the neutrino mass determination, *Physical review letters*, **115**(6), 062501, 2015.

[Fle05] A. Fleischmann, C. Enss, und G.M. Seidel, Metallic Magnetic Calorimeters, *Cryogenic Particle Detection, Topics in Appl. Phys.*, **99**, 151–216, 2005.

[Fog11] GL Fogli, E Lisi, A Marrone, A Palazzo, und AM Rotunno, Evidence of θ 13$>$ 0 from global neutrino data analysis, *Physical Review D*, **84**(5), 053007, 2011.

[Fuk98] Y Fukuda, T Hayakawa, E Ichihara, K Inoue, K Ishihara, Hirokazu Ishino, Y Itow, T Kajita, J Kameda, S Kasuga, et al., Evidence for oscillation of atmospheric neutrinos, *Physical Review Letters*, **81**(8), 1562, 1998.

[Gas17] Loredana Gastaldo, Klaus Blaum, K Chrysalidis, T Day Goodacre, A Domula, Menno Door, H Dorrer, Ch E Düllmann, K Eberhardt, Sergey Eliseev, et al., The electron capture in 163 ho experiment–echo, *The European Physical Journal Special Topics*, **226**(8), 1623–1694, 2017.

[Hen17] D. Hengstler, *Development and characterization of two-dimensional metallic magnetic calorimeter arrays for the high-resolution X-ray spectroscopy*, Dissertation, Kirchhoff-Institut für Physik, Universität Heidelberg, Nov 2017.

[Hol97] G Holzer, M Fritsch, M Deutsch, J Hartwig, und E Forster, K a1, 2 and k b1, 3 x-ray emission lines of the 3d transition metals, *Physical Review-Section A-Atomic Molecular and Optical Physics*, **56**(6), 4554–4568, 1997.

[Jos62] B. D. Josephson, Possible new effects in superconductive tunnelling, *Physics Letters*, **1**(7), 251–253, 1962.

[Kel83] William P Kells und John P Schiffer, Possibility of observing recoilless resonant neutrino absorption, *Physical Review C*, **28**(5), 2162, 1983.

[Kem16] Sebastian Kempf, Anna Ferring, und Christian Enss, Towards noise engineering: Recent insights in low-frequency excess flux noise of superconducting quantum devices, *Applied Physics Letters*, **109**(16), 162601, 2016.

[Koc07] RH Koch, DP DiVincenzo, und J Clarke, Model for 1/f flux noise in squids and qubits, *Physical Review Letters*, **98**(26), 2007.

[Koe18] Katrina E Koehler, Michael A Famiano, Chris J Fontes, Thomas W Gorczyca, Michael W Rabin, Dan R Schmidt, Joel N Ullom, und Mark P Croce, First calorimetric measurement of electron capture in ^{193}Pt with a transition-edge sensor, *Journal of Low Temperature Physics*, **193**(5-6), 1151–1159, 2018.

[Lin07] M. Linck, *Entwicklung eines metallischen magnetischen Kalorimeters für die hochauflösende Röntgenspektroskopie*, Dissertation, Kirchhoff-Institut für Physik, Universität Heidelberg, Mai 2007.

[Pau77] Wolfgang Pauli, *Fünf Arbeiten zum Ausschließungsprinzip und zum Neutrino*, Number 27 in Texte zur Forschung, Wissenschaftliche Buchgesellschaft Darmstadt, 1977, http://neutrino.uni-hamburg.de/...pauli.pdf.

[Ran14] PC-O Ranitzsch, C Hassel, M Wegner, S Kempf, A Fleischmann, C Enss, L Gastaldo, A Herlert, und K Johnston, First calorimetric measurement of oi-line in the electron capture spectrum of ^{163} ho, *arXiv preprint arXiv:1409.0071*, 2014.

[Rob15] RGH Robertson, Examination of the calorimetric spectrum to determine the neutrino mass in low-energy electron capture decay, *Physical Review C*, **91**(3), 035504, 2015.

[SB17] M Shamsuzzoha Basunia, Nuclear data sheets for a= 193, *Nuclear Data Sheets*, **143**, 1–381, 2017.

[Sch94] J Schweppe, RD Deslattes, T Mooney, und CJ Powell, Accurate measurement of mg and al kα1, 2 x-ray energy profiles, *Journal of electron spectroscopy and related phenomena*, **67**(3), 463–478, 1994.

[Tes77] C. D. Tesche und J Clarke, dc SQUID: Noise and optimization, *Journal Of Low Temperature Physics*, **29**(3), 301–331, 1977.

[Tho09] A Thompson, D Attwood, E Gullikson, M Howells, J Kortright, A Robinson, et al., X-ray data booklet (2009), *URL http://xdb. lbl. gov*, 2009.

[Wap85] AH Wapstra und G Audi, The 1983 atomic mass evaluation:(i). atomic mass table, *Nuclear Physics A*, **432**(1), 1–54, 1985.

[Wei96] H Weinstock, Squid sensors: fundamentals, fabrication, and applications, *Kluwer Academic Publishers*, 1996.

Ich versichere, dass ich diese Arbeit selbständig verfasst und keine anderen als die angegeben Quellen und Hilfsmittel benutzt habe.

Heidelberg, 23. Juli 2019 .....

(Tobias Schmitt)